Low hydrogen concentrations in Dharwar cratonic lithosphere inferred from peridotites, Wajrakarur kimberlites field: Implications for mantle viscosity and carbonated silicate melt metasomatism

Jiten Pattnaik, Sylvie Demouchy, Sujoy Ghosh

Low hydrogen concentrations in Dharwar cratonic lithosphere inferred from peridotites, Wajrakarur kimberlites field: Implications for mantle viscosity and carbonated silicate melt metasomatism

Jiten Pattnaik[1], Sylvie Demouchy[2], Sujoy Ghosh[1]*

1. Department of Geology and Geophysics, Indian Institute of Technology Kharagpur, Kharagpur-721302, West Bengal, India.

2. Géosciences Montpellier, Université Montpellier & CNRS, 34095 Montpellier, France.

Accepted for publication in *Precambrian Research*

Cite as Pattnaik, J., Demouchy S., Ghosh, S.K., (2021) Hydrogen concentrations in mantle xenoliths and minerals from Wajrakarur kimberlite field, Eastern Dharwar Craton, India. Precambrian Research, 352, 105982. https://doi.org/10.1016/j.precamres.2020.105982

* corresponding author
Dr. Sylvie Demouchy
Geosciences Montpellier
Univ. Montpellier & CNRS
Place E. Bataillon
34 000 Montpellier
France
sylvie.demouchy@umontpellier.fr

Abstract

Hydrogen as an atomic impurity in mantle minerals is recurrently proposed as a key element impacting significantly on many mantle properties and processes such as melting temperature and mechanical strength. Nevertheless, interpretation based on the natural samples remains weak as we do not have yet a robust world-wild database for hydrogen concentrations in mantle minerals and rocks. Here, we report the first hydrogen concentrations in nominally anhydrous minerals from a rare selection of ultramafic rocks and minerals embedded in Mesoproterozoic Wajrakarur kimberlites (Eastern Dharwar craton, India). Based on key chemical elements, we demonstrate that olivine, pyroxenes and garnet from the Dharwar craton are of mantle origin. We quantify the hydrogen concentrations using Fourier transform infrared spectroscopy (FTIR) and mineral-specific FTIR calibrations. Calculated hydrogen concentrations are, in average, 18 ppm wt H_2O in olivine, 70 ppm wt H_2O in orthopyroxene and 207 ppm wt H_2O in clinopyroxene. Garnet has highly variable hydrogen concentration ranging from 0 to 258 ppm wt H_2O, probably influenced by nano-scale inclusions. The average of clean garnet spectra yields 14.5 ppm wt H_2O. The reconstructed hydrogen bulk concentrations of Dharwar peridotites yields 40^{+10}_{-8} ppm wt H_2O. This value is two to five times lower than the estimated hydrogen concentration in the lithospheric mantle, and agree well with the lower range of hydrogen bulk concentration from the current data base for the upper mantle minerals transported by kimberlites from other cratons (e.g., South Africa, Siberia). The low hydrogen concentration in mantle minerals, together with petrological and geochemical evidence of carbonated silicate melt metasomatism in Dharwar cratonic lithospheric mantle, suggest that these xenoliths are possibly related to proto-kimberlite melts with low water activity prior to being transported to the surface by the Mesoproterozoic Wajrakarur kimberlites. These observations, valid to a depth of ~165-km, suggest that cratonic lithosphere beneath the Dharwar craton may not be particularly indicative of an abnormal hydrogen-rich southern Indian lithosphere in the late Archean and that hydroxylic weakening in olivine would induced a negligible effect on the mantle viscosity of Indian subcontinent.

Keywords: Peridotite xenolith; Wajrakarur kimberlite; Eastern Dharwar craton; hydrogen; FTIR

1. Introduction

Hydrogen (H) can be embedded within the crystallographic lattice of nominally anhydrous minerals (NAMs, such as olivine, pyroxenes, and garnet) as extrinsic points defects (e.g., Beran and Zemman, 1969; Beran and Libowitzky, 2006). Hydrogen incorporation, even at a low concentration level (expressed in part per million of water by weight in this study) is known to enhance many physical and chemical properties of mantle minerals and rocks. For example, a small amount of H can increase electrical conductivity (Karato, 1990; Yoshino et al., 2006; Poe et al., 2010; Novella et al., 2017; Sun et al., 2019; Fei and Katsura, 2020) or increase ionic diffusion of major elements in mantle minerals (e.g., Costa and Chakraborty 2008; Demouchy et al., 2007). Furthermore, the incorporation of H was also proposed to weaken the strength of single crystal and polycrystalline olivine (e.g., Mackwell et al., 1985; Hirth and Kohlstedt, 2003; Demouchy et al., 2012; Tielke et al., 2017). As a consequence, distribution of H in the upper mantle minerals is repetitively proposed as a major parameter in geodynamic models (e.g., Regenauer-Lieb and Kohl, 2003; Regenauer-Lieb et al., 2006; Albarède, 2009; Peslier et al., 2010; Masuti et al., 2016).

Laboratory experiments have been crucial to understand the primary mechanisms of incorporation of H in mantle silicates at point defects scale and also to quantify the 'water solubility' in mantle minerals as a function of thermodynamic parameters (e.g., Bali et al., 2008; Férot and Bolfan-Casanova, 2012; Gaetani et al., 2014; Keppler and Bolfan-Casanova, 2006; Kohlstedt et al., 1996; Mierdel et al., 2007; Mierdel and Keppler, 2004; Padrón-Navarta and Hermann, 2017). Although, it has long been known that almost all natural NAMs contain variable amounts of H in their structures (Beran and Libowitzky, 2006; Litasov et al., 2007; Skogby, 2006). Furthermore, the systematic characterization and quantification of H concentrations in upper mantle minerals from mantle peridotites of different geological settings have been explored in the last two decades (see Peslier, 2010; Demouchy and Bolfan-Casanova,

83 2016 for reviews). Mantle xenoliths and large phenocrysts hosted by kimberlites in cratonic
84 settings have received most of the attention regarding their H concentrations (e.g., Bell and
85 Rossman, 1992a; 1992b; Bell et al., 2004; Grant et al., 2007; Peslier et al., 2008, 2010, 2012;
86 Baptiste et al., 2012), with undeniable popularity for the Kaapvaal craton, South Africa. Several
87 studies are also available for the Siberia craton (Matsyuk et al., 1998; Matsuyk and Langer,
88 2004; Koch-Mueller et al., 2006; Schmädicke et al., 2013; Doucet et al., 2014; Taylor et al.,
89 2016, Jean et al., 2016). The literature has reported astonishing NAMs inclusions in diamonds,
90 which also permit to further constrain the H concentration in the Earth's upper mantle (e.g.,
91 Kurosawa et al., 1997; Matsyuk and Langer, 2004; Novella et al., 2015; Taylor et al., 2016;
92 Jean et al., 2016).
93 To date, available literature data only reports four H concentrations in nominally anhydrous
94 mineral specimens from the Indian subcontinent: (1) one garnet from an unknown geological
95 setting in Maldener et al., 2003 (sample # RAJA, $Prp_{42}Alm_{54}Sps_2Grs_2$, 14 ppm wt H_2O); (2)
96 large gem-quality metamorphic diopsides from Jaipur (Rajasthan) recurrently used for diffusion
97 experiments (i.e., sample # CIT. 11221 in Skogby et al., 1990 ; Skogby and Rossman, 1989;
98 Carpenter Woods et al., 2000; Ferriss et al., 2016); (3) an augite from Kangan area, Andhra
99 Pradesh (i.e., sample # GRR 1660, Skogby et al., 1990), and (4) two metamorphic enstatites
100 (i.e., samples GRR1650a,b; Skogby et al., 1990). Nevertheless, none of these nominally
101 anhydrous mineral specimens have a confirmed mantle origin, thus no statement can be
102 proposed regarding the hydrogenation state and strength of the continental mantle lithosphere
103 of any part of Indian subcontinent.
104 Here, we report the first detailed measurements of H concentrations, major and key
105 minor and trace element concentrations in NAMs (olivine, orthopyroxene, clinopyroxene and
106 garnet) from spinel- and garnet-bearing peridotite xenoliths and olivine grains embedded in
107 kimberlites from the Wajrakarur kimberlite field in the Eastern Dharwar craton, India.

Moreover, we also report H contents in several fresh garnet and clinopyroxene single crystals which were separated from Wajrakarur kimberlite-hosted peridotite xenoliths. Our main aim is therefore to quantify the H content in mantle NAMs beneath the Eastern Dharwar craton.

2. Material and Methods

Previous studies by Ganguly and Bhattacharya (1987) and Nehru and Reddy (1989) already described the petrography of peridotitic mantle xenoliths hosted by Proterozoic Wajrakarur kimberlites from the Eastern Dharwar craton and calculated the equilibrium pressures and temperatures of these samples. The more recent study by Pattnaik et al. (2020) focused on trace element compositions of olivine, garnet, clinopyroxene, orthopyroxene, spinel and ilmenite of a larger selection of ultramafic xenoliths from the same area. Here we mainly focus on the quantification of H in NAMs from selected peridotite mantle xenoliths and mantle minerals hosted in Group-II kimberlites (orangeites) from the Wajrakarur kimberlite field in the Eastern Dharwar craton, India. Please note that Group-II kimberlites (orangeites) are recently being classified as a variety of lamproite (Pearson et al., 2019). The geological context of the Dharwar craton and Wajrakarur kimberlite field is briefly presented below.

The Archean Dharwar craton represents a classical granite-greenstone terrane which is overlaid on a basement of tonalite-trondhjemite-granodiorite gneisses (Naqvi and Rogers, 1987). The Dharwar craton is bounded in the east by the Proterozoic Eastern Ghats Mobile Belt, in the northeast by the Archean Bastar craton and in the northwest by the cretaceous-tertiary Deccan traps. The Dharwar craton is divided into the Eastern Dharwar craton (EDC) and the Western Dharwar craton (WDC) by the Chitradurga boundary fold, which is considered as a distinct shear zone (Chadwick et al., 2000; Ramakrishnan and Vaidyanadhan, 2010).

The kimberlite pipes in the Dharwar craton are mainly confined to the Eastern part and are distributed in three fields as illustrated in Figure 1: *Wajrakarur kimberlite field* (~80 × 70

133 km), situated in the southern part of the EDC, approximately at 400 km east of Goa and 200 km
134 north of Bangalore (Anantapur district, Andhra Pradesh); the *Narayanpet kimberlite field* in the
135 northern part of the EDC, and at last the *Raichur kimberlite field* located between the other
136 fields. In the *Wajrakarur field*, there are more than 30 individual pipes spread over four distinct
137 clusters: *Wajrakarur-Lattavaram*, *Chigicherla, Kalyandurg* and *Timmasamudram* (Nayak and
138 Kudari, 1999). Kimberlites from the Wajrakarur field are poorly diamondiferous, while the
139 other fields are diamond-free (Ravi et al., 2013). Ages based on $^{40}Ar/^{39}Ar$ and U–Pb isotope
140 systems on separate grains of phlogopite and crustal perovskite indicate that kimberlite
141 emplacement occurred around 1.1 Ga (Gopalan and Kumar, 2008; Osborne et al., 2011;
142 Chalapathi Rao et al., 2014; see also study on major and trace element compositions of
143 clinopyroxenes and garnets in Shaikh et al., 2020).
144 The magmatic intrusions in the Wajrakarur field are mostly kimberlites, while some are
145 lamproites or orangeites, and ultramafic lamprophyres (Smith et al., 2013). A detailed account
146 of the mode of occurrence and features of the individual pipes of Wajrakarur kimberlite field is
147 given by Neelkantam (2001), Ravi et al. (2009) and Fareeduddin and Mitchell (2012). The
148 magmatic rocks contain peridotites, eclogites and crustal xenoliths as well as megacrysts
149 (Ganguly and Bhattacharya, 1987; Nehru and Reddy, 1989; Karmalkar et al., 2009). In the
150 Kalyandurg cluster eclogites dominate the mantle xenolith population (95%).
151
152 **2.1. Samples description**
153 The studied samples are olivine (ol), orthopyroxene (opx), clinopyroxene (cpx) and
154 garnet (grt) from two fresh mantle xenoliths: one spinel (±garnet)-lherzolite (sample P3/5/1)
155 and one garnet-lherzolite (sample P3/6/1); and mantle olivines within a kimberlitic matrix
156 (sample P3/6/3), all from pipe 3 (Fig. 1). We also selected 10 garnets and 15 diopsides fresh
157 single grains, which were hand-separated from crushed xenoliths from different pipes of the

158 Wajrakarur kimberlite field (pipes 1, 3, 6, 7 and 10; Fig. 1). Unfortunately, satisfying grains of
159 olivines and orthopyroxenes could not be recovered from crushed peridotites.
160 All the samples are from the *Wajrakarur-Lattavaram* cluster (Fig. 1) and the samples
161 description is summarized in Table 1. The mineral modal compositions were calculated using
162 a free image processing software ImageJ v.152 for two lherzolites (samples P3/5/1 and P3/6/1)
163 and yield: $Ol_{77}Opx_{15}Cpx_{7}Sp_{1}$ (garnet<<0.5) for sample P3/5/1, and $Ol_{74}Opx_{13}Cpx_{9}Grt_{4}$ for
164 sample P3/6/1. Modal compositions of these two samples are reported in Table 1. Equilibrium
165 temperatures were calculated using the classical two-pyroxenes geothermometer by Brey and
166 Köhler (1990) for a hypothetical initial pressure of 4 GPa. It yields 3.0 GPa of pressure and a
167 temperature of 940 °C for sample P3/5/1; 4.5 GPa of pressure and a temperature of 1050 °C for
168 sample P3/6/1 and; 5.5 GPa of pressure and a temperature of 1270 °C for sample P3/6/3 (Table
169 1). Furthermore, following recommendations by Nimis and Grutter (2010), two-pyroxenes
170 thermometer by Taylor (1998) was also used to calculate the equilibration temperatures (T_{TA})
171 with an assumed initial pressure of 3 GPa for spinel peridotites and 5 GPa for garnet peridotites.
172 The estimated equilibration temperatures for theses peridotite give lower temperature ranging
173 from 710 to 1179 °C. Furthermore, garnet-orthopyroxene geobarometer based on aluminum
174 exchange was taken into consideration by Nickel and Green (1985) for calculating the
175 equilibration pressures with T_{TA} values set as the initial temperatures, which yield a pressure
176 range of 2.5-5.0 GPa.
177 The peridotite xenoliths are coarse-grained, with olivine grain size between 2 and 7 mm,
178 orthopyroxene grain size up to 3 mm, clinopyroxenes have grain size between 2 and 7 mm,
179 garnets have grain size below 2 mm, and spinel below 1 mm, as illustrated in Fig. 2. The olivines
180 and orthopyroxenes do not show undulose extinction or specific features of plastic deformation.
181 Nevertheless, the rock sections are commonly fractured (Fig. 2), probably due to rapid ascent
182 toward the surface. The clinopyroxenes are of irregular shape and mainly intergranular and thus

183 are likely formed after the olivines and orthopyroxenes. Garnets have subhedral to anhedral
184 shape with no apparent chemical zoning and some garnets are embedded in clinopyroxene.
185 Spinels are intergranular with typical holly-leaf shape.
186
187 **2.2. Electron probe micro-analyzer**
188 The chemical compositions of the mantle-derived minerals were analyzed using a
189 Cameca SX-100 electron probe micro-analyzer (EPMA) wavelength dispersive spectroscopy
190 (WDS) at Department of Geology and Geophysics, Indian Institute of Technology (IIT)
191 Kharagpur (India). Analytical procedures were performed with a 15 kV accelerating voltage
192 and 20 nA probe current on regular 30-μm thin sections. The measuring peak and background
193 times were 20 s and 10 s, respectively. The oxides and silicates standards used for the EPMA
194 calibration were orthoclase (Si, K), rutile (Ti), chromite (Cr), corundum (Al), hematite (Fe),
195 rhodonite (Mn), periclase (Mg), diopside (Ca), jadeite (Na). The number of point analyses per
196 mineral grain range from 3 to 25 (further analytical details are given in Pattnaik et al., 2020).
197 Homogeneity was checked by comparing core to rim composition. Mg# was calculated as equal
198 to 100×Mg/(Mg+Fe) in atomic ratio, whereas Cr# in spinel was calculated as 100×Cr/(Cr+Al).
199 The typical EPMA results are reported in Table 2.
200
201 **2.3. Laser ablation inductively coupled plasma mass spectrometer**
202 Laser ablation inductively coupled plasma mass spectrometer (LA-ICP-MS)
203 measurements for minor and trace elements in olivine, clinopyroxene, and garnet were carried
204 out using a Thermo Fisher Scientific ICAP-Q quadrupole ICP-MS combined to a New Wave
205 193 ArF Excimer laser ablation system at Department of Geology and Geophysics, IIT
206 Kharagpur, India. The laser was used with an energy density of 5 J/cm^2 at a frequency of 5 Hz
207 and using a spot size of 50 μm. The ICP-MS was perfected for maximum sensitivity for Li and

208 Th using the NIST 612 as a reference glass. The oxide production rate was monitored using
209 $^{232}Th^{16}O$ and was below 1.0-1.2 %. The analyses were performed in time-resolved mode with
210 each analysis consisting of 35 seconds of background measurement with the laser turned off
211 followed by 45 seconds peak signal measurement while the laser was ablating the sample.
212 External standardization was obtained by the bracketing group of two measurements of NIST
213 612. The data quality was monitored by measuring the NIST 610 reference glass as unknown
214 interspersed with the measurements of the samples. The raw data were reduced using the
215 GLITTER® software, with SiO_2 as an internal standard from electron microprobe analyses for
216 olivine and pyroxenes, and CaO for garnet, and carefully inspected against heterogeneities in
217 the analyzed volume. Analyses were performed on a thin polished section for the rock slabs and
218 epoxy mounts for the mineral separates. Only unaltered and crack-free mineral grain areas were
219 analyzed. For each mineral, 1 to 6 analyses were performed within the grain cores. Here, we
220 only focused on minor and trace elements known to form major associated point defect with H
221 (e.g., Ti in olivine, e.g., Padrón-Navarta and Hermann, 2017), or coupled incorporation (Li,
222 e.g., Kent and Rossman, 2002) or to have similar incompatible behavior (e.g., according to
223 Dixon et al., 2002, between La and Ce) and common divalent ions not obtained accurately by
224 EPMA (Ni, Mn, Na, Ti). These concentrations are also reported in Table 2.
225
226 **2.4 Fourier transform infrared spectroscopy**
227 Hydrogen in mantle minerals was detected and quantified using transmission Fourier
228 transform infrared spectroscopy (FTIR) spectroscopy at the Laboratoire Charles Coulomb
229 (University of Montpellier, France). Rock thick sections (samples P3/5/1, P3/6/1 and P3/6/3)
230 and separated grain were hand-polished with diamond lapping films (grid size from 30 μm to
231 0.5 μm) down to a thickness ranging from 211 to 590 μm. The final thickness for each sample
232 is reported in Table 3. To preserve the microstructures, the crystals were not

crystallographically oriented, and thus only unpolarized infrared spectra were acquired using a Bruker IFS66v spectrometer, equipped with a liquid nitrogen-cooled MCT detector (Mercatel alloy, HgCdTe), a KBr/Ge beam splitter. The spectrometer was coupled to a Bruker HYPERION microscope. Unpolarized IR measurements were performed following the protocol of Demouchy et al. (2019): A square aperture (100 × 100 μm) was used, only optically clean zones, free of cracks or inclusions, of the mineral grains were chosen for analyses, and over 200 scans were accumulated at a resolution of 4 cm^{-1}. Each spectrum was baseline corrected (using OPUS software or subsequently, if needed, using the spline function in Igor Pro), and the absorbance was normalized to 1 cm thickness to yield the absorption coefficient.

We used two different types of infrared calibrations to calculate H concentrations: (1) the classic empirical frequency-dependent calibration of Paterson (1982) for unpolarized infrared and (2) mineral-dependent calibrations (Bell et al., 1995, for pyroxenes and garnet; Withers et al., 2012, for olivine). The frequency-dependent calibration of Paterson (1982) is given as

$$C_{OH} = \frac{\chi i}{150\zeta} \int \frac{\mathrm{k}(\upsilon)}{3780 - \upsilon} d\upsilon$$

Where the following mineral specific factors χ_i (Paterson, 1982) were used, and adjusted as a function of the chemical composition in major element of the mineral *i* and thus its density (see method of calculation in Demouchy and Bolfan-Casanova, 2016): χ_{ol} = 2718 or 2726 ppm wt H_2O for $Fo_{92.2}$ or $Fo_{93.3}$, respectively; χ_{Opx} = 2727 ppm wt H_2O, χ_{Cpx} = 2695 or 2714 ppm wt H_2O, for P6 or P1P2, respectively and χ_{garnet}= 2326 ppm wt H_2O for an average composition close to $Prp_{76}Alm_{12}Sps_1Grs_{11}$; ζ is the orientation factor and equals 1/3 for unpolarized infrared analyses (here on non-crystallographically oriented grains, see Paterson, 1982 for details); and k(υ) the absorption coefficient is a function of the wavenumber υ. Typical integration of the spectrum ranges from 3620–2900 cm^{-1} for olivine, 3700–3000 cm^{-1} for pyroxeness and garnet, and was slightly adjusted if necessary (e.g., ± 10 cm^{-1}). Note that when

concentration obtained by unpolarized infrared are multiplied by a factor three, it yields satisfying estimate compare to the sum of concentrations obtained by polarized infrared for the three crystallographic directions (see suppl. Fig. S1 in Férot and Bolfan-Casanova, 2012). This calibration allows a detection limit of about 1 ppm wt H_2O for a 1-mm-thick olivine sample (Demouchy and Mackwell, 2003, 2006). The estimated error from the empirical calibration in the resulting H concentration is around 30% (Paterson, 1982; Rauch, 2000), but lower for the olivine calibration of Withers et al. (2012). Note that the maximum linear absorbance of the non-normalized spectrum did not exceed 0.3, in agreement with the recommendations of Withers et al. (2012) for unpolarized FTIR measurements of olivine. Also, if possible, at least 10 spectra of different orientation should be average to improve accuracy of the measurements (Kovàcs et al., 2008). Here is was only possible for the PIP2 diopsides. The normalized integrated area (absorption) are also reported for application to future IR mineral-dependent calibrations or to previous calibrations (for olivine Bell et al., 2003, which overestimate H content, see Withers et al., 2012 for discussion).

3. Results

3.1 Summary of major and minor elements

Major element compositions are reported in Table 2 for olivines, orthopyroxenes, clinopyroxenes and Al-rich phases (garnet or spinel). They are used to infer mineral petrogenetic origin and to further investigate potential variations in H as a function of major element concentrations. Only a selection of minor and trace elements is reported here (Ni, Mn, Na, Ti, La, Ce, Li, V) which are recurrently proposed as potentially associated point defects with proton in olivine (e.g., Ti-clinohumite-like point defect, Padrón-Navarta et al., 2014;

283 Padrón-Navarta and Hermann, 2017) or orthopyroxenes (e.g., Al-H coupled substitution,
284 Mierdel et al., 2007) or having a chemical behavior similar to H.
285
286 *Olivine*
287 Olivines have relatively homogeneous composition with high Mg# ranging between
288 92.4 and 93.4. The compositions in FeO and CaO range from 6.8-7.6 wt.% and 0.02- 0.04 wt.%,
289 respectively. Contents in Ni range from 2932-2942 ppm. The Mg# data from this study and
290 other olivine samples from the Dharwar craton are inversely but weakly correlated with NiO
291 contents as illustrated in Figure 3a. The concentrations in Ti and V vary from 34-93 ppm and
292 2.4-5.6 ppm respectively. The Li concentration was too low to be determined in olivine (< 4
293 ppm).
294
295 *Orthopyroxene*
296 The concentration of orthopyroxene is quite homogeneous within grains with MgO and
297 FeO contents ranging from 36-37 wt.% and 4.3-4.6 wt.% respectively. The orthopyroxenes are
298 enstatite with Mg numbers ranging from 93.3 to 93.9, which is typical for mantle-derived
299 orthopyroxene (Dick and Bullen, 1984). The Cr# varies between 17.7 and 18.7, with Cr_2O_3
300 contents ranging from 0.31 to 0.33 wt.%. The contents in CaO and MnO range from 0.2 to 0.4
301 wt.% and 0.08 to 0.11 wt.%, respectively, while Al_2O_3 contents are very low in these
302 orthopyroxene samples (0.96 wt.%, Table 2).
303
304 *Clinopyroxene*
305 Clinopyroxenes are mostly Cr-diopsides with 1.0-2.6 wt.% Cr_2O_3, except for sample
306 P3/5/1 (spinel-bearing peridotite) and P3 grain, which have a very low Cr_2O_3 content (0.25
307 wt.% and 0.6 wt.%, respectively, see Table 2). The Mg# and Cr# vary from 91.35 to 93.55 and

24.4 to 32.3, respectively, whereas in case of P3 and P6 grains the Cr# is 16.71 and 42.20, respectively. The MgO and FeO contents range from 16.3–20.5 wt.% and 2.15–3.0 wt.%, respectively. The CaO, Al_2O_3, and Na_2O contents vary from 17.79-23.6 wt.%, 0.52-3.2 wt.%, and 0.5-2.4 wt.%, respectively. The TiO_2 content and Mg# of clinopyroxenes from the studied xenoliths show a weak negative correlation (Fig. 3b, R^2=0.83) if the clinopyroxene grain from P1P2 is excluded. Indeed, the latter sample is also at odds this the current database as shown in Fig 3b. The CaO and Al_2O_3 contents of clinopyroxenes are also weakly correlated (R^2=0.73) as shown in Fig 3c, if clinopyroxene from sample P3/5/1 is discarded which has a CaO content very low compare to the rest of the database.

Spinel

Spinels are present only in sample P3/5/1 and display Mg# of ~ 64.8, and Cr# of ~ 67.6 with MgO and Cr_2O_3 contents are 13.9 wt.% and 53.8 wt.%, respectively (Table 2). The Al_2O_3 and FeO contents are also homogeneous within the sample with 17.3 wt.%, and 14.9 wt.%, respectively. The Mg# of olivine together with the high Cr_2O_3 contents still place these spinel in the olivine-spinel mantle array (OSMA, Arai, 1994), although in the cratonic subgroup (e.g., Tran and Nguyen, 2018).

Garnets

Garnets are homogeneous with no distinct compositional variation from the core to rim. The Mg# and Cr# range from 84.6- 85.8 and 5.1- 7.5, respectively for the garnets group P1P2, P3D and P3B. Compare to other garnets from this study, P7 garnets have high Cr# ranging from 14.8- 23.7. We have further separated P7 garnets individually (P7-1 and P7-2, see Table 2). Using the classic negative correlation between Al_2O_3 and Cr_2O_3 contents as a petrogenetic indicator, it confirms that our samples have mantle peridotite origin, as such relation is never

observed for mantle eclogites as illustrated in Fig 3d. The Al_2O_3 and CaO contents range from 17.5- 22.3 wt.% and 4.2 - 5.1 wt.%, respectively, which are also typical for the peridotitic garnets (e.g., Ingrin and Skogby, 2000; Peslier, 2010). The Cr_2O_3 content lies in the range of 1.8 to 2.6 wt. % for lherzolitic garnets while in case of harzburgitic garnets, P7G1 and P7G2, it varies from 5.1 to 8.1 wt.% and P10 is just between these latter values with a concentration of 6.9 wt.% Cr_2O_3. The content in Ti and Ni vary from 1280- 2544 ppm and 30-111 ppm, respectively, while the Ti concentrations are low (<300 ppm) in P7 garnets.

3.2 Fourier transform infrared spectra

Over 182 analyses were performed by FTIR, unfortunately only a handful of spectra could be used to providing accurate estimates of H distribution and concentration in mantle nominally anhydrous minerals from Wajrakarur kimberlite field. Despite optical clearness, many grains were altered, and contamination by hydrous minerals lamellae (e.g., serpentine and amphibole) or along cleavages prevented accurate detection and quantification of H. The unpolarized FTIR spectra of uncontaminated olivine, pyroxenes and garnet are shown in Figure 4. Examples of contamination by lamellae of hydrous minerals are shown in Figure 5, where the strong absorption band at 3686 cm^{-1} corresponds to structural OH groups in serpentines (Miller et al. 1987; Post and Borer 2000; Baptiste et al. 2012) and 3670 cm^{-1} OH groups in amphibole (Skogby, 2006).

The spectra of olivine grains show distinct FTIR features: these olivine grains within the kimberlitic matrix in sample P3/6/3 have typical mantle-derived spectra with absorption bands at 3600, 3572, 3525 and 3227 cm^{-1} (Demouchy and Bolfan-Casanova, 2016).

The spectra of orthopyroxenes (P3/5/1) display OH bands located at 3602, 3548, 3517, 3409, 3313, and 3052 cm^{-1}. While the bands at 3602, 3517, 3313, and 3052 cm^{-1} are typical of

hydrogen-rich mantle-derived orthopyroxenes, the band at 3542 cm^{-1} is not easily found in other mantle-derived orthopyroxene, even when hydrogen content is low (Fig. 4c).

The spectra of Dharwar peridotitic clinopyroxenes display three major bands, again typical of mantle-derived diopsides located at 3640, 3530 and 3444 cm^{-1} (Fig. 4b, Ingrin and Skogby, 2000; Skogby, 2006; Peslier, 2010, Demouchy and Bolfan-Canova, 2016).

Garnets, despite excellent clarity and large grain size (> 2 mm), do not show typical hydroxyl absorption bands. Only three samples (P1P2, P7, P3/6/1, Fig. 4c) show broad absorption bands at 3630-3622 cm^{-1} and 3427 cm^{-1}. The first band positions match the typical hydrogarnet substitution mechanism (e.g., 4 H^+ occupying a Si vacancy, Geiger and Rossman, 2018; Mookherjee and Karato, 2010). However here the band at 3630-3620 cm^{-1} which is notably broad and do not display the usual well-defined Lorentzian shape for hydrogarnet substitution. The absorption band around 3427 cm^{-1} could be linked to molecular water in micro- to nano-inclusions (e.g., Rossman and Aines, 1991; Bell and Rossman, 1992b; Matsyuk and Langer, 2004, Xia et al., 2005; Sheng et al., 2007).

Peridotites-derived garnets transported in alkali basalts are typically H-free, only mantle-derived garnets hosted by kimberlite display absorption bands at 3571 and 3512 cm^{-1} often linked to Ti-rich composition (Bell and Rossman, 1992a, 1992b; Beran and Libowitzky, 2006 see their Fig. 8; Kurosawa et al., 1997). It is interesting to note that the absence of H in peridotitic garnets equilibrated at depths greater than 80 km is unusual (Bell et al., 1995; Withers et al. 1998; Peslier et al., 2012), while H-free or low H concentrations in garnet inclusions in diamonds were reported in a number of studies (e.g., Novella et al., 2015; Taylor et al., 2016). At last, the infrared features of the Dharwar peridotite garnets do not match either the typical FTIR spectra of eclogitic garnets (see Fig. 7 in Beran and Libowitzky, 2006).

3.3 Hydrogen concentrations

Hydrogen concentrations, expressed in ppm by weight of H_2O and quantified using several calibrations are reported in Table 3. Following the calibration of Paterson (1982), the H concentration ranges from 7-18 ppm wt H_2O in olivine, 53-77 ppm wt H_2O in opx, 41-309 ppm wt H_2O in cpx, and 0–75 ppm wt H_2O in garnet (Table 3). Conversion to atomic ratio $H/10^6$ Si (= ppm H/Si), which is commonly used in mineral physics community, is achieved by multiplying the concentration in ppm wt H_2O by a factor of 16.16 for olivine (for $Fo_{92.5}$, see calculation method in Demouchy and Bolfan-Casanova (2016) for other mineral phases, cf. their Table 1). As the calibration of Paterson (1982) underestimated the H concentrations (Bell et al., 2003; Withers et al., 2012), we also give the concentrations using mineral-dependent calibrations and it yields 11–29 ppm wt H_2O in olivine, 56-88 ppm wt H_2O in opx, 81-642 ppm wt H_2O in cpx, and 0–258 ppm wt H_2O in garnet (see Table 3, details of calibrations are given in section 2.4). Note that if abnormal spectra for garnet are excluded, it yields an average of 14.5 ppm wt H_2O in garnet. Nevertheless, note that the IR bands for our garnets are not perfectly matching the IR spectra of the two garnets used as standards in the calibration by Bell et al. (1995). The same issues applied for the synthetic and very hydrous high pressure olivines used by Withers et al. (2012).

4. Discussion

4.1. Incorporation of hydrogen in upper mantle minerals

Since hydrogen is embedded as atomic impurities in point defects within the structure of NAMs, its incorporation is dependent of the intrinsic parameters (pressure, temperature, and also oxygen fugacity) including chemical composition (e.g., Fe, Ti, Al), which leads to coupled or associated point defects (e.g., Nakamura and Schmalzried, 1983; Mackwell and Kohlstedt, 1990; Berry et al., 2005). Here, the effect of iron can be deciphered using Mg# of the mantle-

derived olivines from the Dharwar craton and they are within the cratonic mantle database as illustrated in Figure 6. Nevertheless, the H concentrations in olivine reported in this study agrees with other Mg-rich and garnet-bearing peridotitic olivines from cratonic (>2.5 Ga) mantle lithosphere (Fig. 6 and Demouchy and Bolfan-Casanova, 2016). It confirms that olivines from spinel-bearing peridotite from off-cratonic settings have lower Mg# (90.4) than olivines cratonic garnet-bearing peridotites (Figure 6, P3/5/1 olivine = Mg# 93.3 and P3/6/1 olivine = Mg# 92.4), but indistinctly with low to high hydrogen concentrations.

Another notable mechanism incorporation mechanism of H in mantle olivine is the association with Ti as a complex (coupled) point defect (PD): the occupancy of Mg vacancy by Ti^{4+} is balanced by $2H^{+}$ incorporation in Si vacancy in olivine (abbreviated henceforth $[Ti\text{-}H]_{PD}$ e.g., Berry et al., 2005; Walker et al., 2007; Padrón-Navarta et al., 2014; Padrón-Navarta and Hermann, 2017; Tollan et al., 2018). This mechanism is characterized by a positive correlation between the absorption of IR bands at 3575 and 3525 cm^{-1} and Ti concentration (at saturation) as shown in Figure 7a. Furthermore, the low Ti and H concentrations of olivine from sample P3/6/3 agrees very well with the current database for mantle-derived olivines as illustrated in Fig. 7b.

In pyroxenes, at low pressure (<5 GPa) and based on experimentally hydrogenated enstatite, Al^{3+} is commonly considered as a H incorporation enhancer (e.g., Rauch, 2000, Mierdel et al., 2007; Stalder, 2004; Stalder et al., 2005; Stalder and Ludwig, 2007; Stalder et al., 2015; Tenner et al., 2009; O'Leary et al., 2010; Férot and Bolfan-Casanova, 2012; Gaetani et al., 2014; Novella et al., 2014). Here, we could not analyze the hydrogen concentration of orthopyroxenes with different alumina content (only in P3/5/1, 0.96 Al_2O_3 wt.%) by FTIR, but fresher clinopyroxenes were available and large enough to yield statistically relevant H concentrations (Fig. 4b and Table 3). The different fields of eclogitic cpx, peridotitic cpx transported in basalts, and kimberlites of mantle origin are easily identified by Al_2O_3 contents

of cpx (cf. dotted lines in Fig. 8), it supports the petrogenetic origin of peridotitic diopsides from the Dharwar craton.

Hydrogen concentrations in garnet are very heterogeneous (0-258 ppm wt H_2O) and comparison of chemical composition among different garnets does not reveal significant variation in Al_2O_3, CaO, or Ti concentrations potentially resulting from metasomatism and explaining the abnormal FTIR spectra. At present, we cannot rule out the possibility of hydroxyl-rich alteration or local contamination by nano-scale inclusions in P1P2 and P3/6/1 garnets (Bell and Rossman, 1992b; Beran and Libowitzky, 2006).

We must also mention the potential re-hydration by the volatiles-rich kimberlitic magma during transport toward the surface: as shown experimentally by Baptiste et al. (2015), the co-existence of CO_2 and H_2O in kimberlitic magma lead to an effective decrease in water fugacity, which does not promote hydrogen incorporation in olivine, or other NAMs. At the opposite, transport within kimberlitic magma also does not seem to promote notable dehydration during ascent, probably due to local point defect interactions and long-term hydrogen locking in peculiar point defects (Thoraval and Demouchy, 2014; Thoraval et al., 2019).

4.2. Reconstructed hydrogen whole-rock concentrations

Despite the limited number of mantle minerals successfully analyzed in this study, we can attempt to estimate, for the first time, the whole-rock (bulk) H concentration of the late Archean Dharwar cratonic lithosphere (3.6-2.5 Ga; Jayananda et al., 2018). Using the estimated mineral modes (a lherzolite with ol: 74%, opx, 14%, cpx 9%, grt 4%, from Table 1) and the average hydrogen concentrations obtained from mineral-specific calibrations (Table 3, 18 ppm wt H_2O in olivine, 70 ppm wt H_2O in opx, 207 ppm wt H_2O in cpx and 14.5 ppm wt H_2O in garnet (based on clean spectra of P1P2-garnet 2 and P7 garnet 3, thus excluding the potentially

contaminated garnets), bulk H concentration yields 40 ppm wt H_2O. Furthermore, we can use experimentally determined partition coefficients of hydrogen for coexisting olivine, orthopyroxene and clinopyroxene to cross-check if this estimate is indicating equilibrium hydrogen concentration distribution. Here, we use the following published partition coefficients from Demouchy et al. (2017): (1) partition coefficients of hydrogen between orthopyroxene and olivine ($D^{opx/ol}$) = 5, (2) partition coefficients of hydrogen between clinopyroxene and orthopyroxene ($D^{cpx/opx}$) = 2, and (3) partition coefficients of hydrogen between clinopyroxene and olivine ($D^{cpx/ol}$) = 10, which were obtained at pressure and temperature ranges as close as possible to the equilibrium conditions of our samples (3 GPa and 1100 °C) for a mantle-derived composition and importantly for a basaltic melt-free system. Indeed, most of the experimental studies have focused on basaltic melt-bearing systems, and a recent compilation can be found in Demouchy et al. (2017, see their Table 3). Since, there is no experimental data for partition coefficient of H between olivine and garnet ($D^{ol/grt}$) in a basaltic melt-free system, we decided to use an average value of $D^{ol/grt}$=0.65, calculated using the results of experimental studies on hydrous lherzolites ($D^{ol/grt}$=0.6 from Gaetani and Grove, 1998; $D^{ol/grt}$=0.7 recalculated from Hirschmann et al., 2009). Temperature and pressure conditions of these experiments are fairly close to those of our samples. These experimental values are also close to the previous estimates of partition coefficient of H between olivine and garnet in MORB composition (e.g., $D^{ol/grt}$=1, Hirth and Kohlstedt, 1996). Using these partitioning coefficients, the same mineral mode (ol: 74%, opx, 14%, cpx 9%, grt 4%) and the hydrogen concentration in olivine as a reliable concentration, it yields 41 ppm wt H_2O, thus in agreement with the first estimate given above. If opx or cpx is used as the initial concentration, it yields 32 or 48 ppm wt H_2O, respectively. These estimates permit to further constrain the bulk H concentration to 40^{+10}_{-8} ppm wt H_2O.

The bulk H concentration in the Dharwar cratonic lithosphere is four to five times lower than the geochemical estimates of bulk H concentration in the upper mantle, e.g., 150 ppm wt

H_2O (Michael, 1988; Saal et al., 2002; Marty, 2012), H concentration in peridotites from lithospheric mantle (150-200 ppm wt H_2O; Demouchy and Bolfan-Casanova, 2016). This bulk hydrogen concentration is also well below saturation values of H concentration reported by experimentation at lithospheric conditions, i.e. ~ 700 ppm wt H_2O. (at 220 km of depth, see Férot and Bolfan-Casanova, 2012). However, together with the equilibrium pressure estimates, the resulting H concentrations in olivine from the Dharwar craton (Fig. 9) agree well with the lower range of the current database for H-rich mantle olivines transported by the kimberlitic magmas (e.g., South Africa and Udachnaya; Peslier et al., 2010; Baptiste et al., 2012; Doucet et al., 2014).

4.3. Role of metasomatism

Metasomatism might be considered as a mantle process inducing enrichment or depletion of H in the mantle NAMs (e.g., Bell and Rossman, 1992a; Ingrin and Skogby, 2000; Peslier et al., 2012; Denis et al., 2015; Demouchy et al., 2015: Satsukawa et al., 2017). On the contrary, undersaturated partial melting and melt extraction can only induce H extraction as H is an incompatible element (e.g, Dixon et al., 2002). As mentioned above, the estimated bulk H concentration of Dharwar peridotites is 40^{+10}_{-8} ppm wt H_2O is much lower than the current estimates for the Earth's upper mantle (e.g., 150 ppm wt H_2O, Michael, 1988; Saal et al., 2002; Marty, 2012; Demouchy and Bolfan-Casanova, 2016). Such low H concentrations could also be linked to (1) melting-induced depletion, as the depleted peridotites from the Dharwar craton probably represent a mantle residue after ~35-50 % melting, as suggested by Pattnaik et al. (2020), or (2) melt-rock interactions as suggested in the irregular REE_N patterns in peridotitic clinopyoxenes from the Dharwar craton (Pattnaik et al., 2020) or as shown by a study on Japan back arc system, e.g. Oki-Dogo locality (SW Japan, Satsukawa et al., 2017). These low H

concentrations, together with trace element enrichment in clinopyroxenes, are indeed the accurate witness of significant melt-rock interactions (Pattnaik et al., 2020). They have a different signature than results from cryptic metasomatism (e.g., Ichinomegata peridotites, which preserved or enhanced the H concentrations in pyroxenes (Satsukawa et al., 2017). Here, in Figure 8, the hydrogen and alumina compositions of clinopyroxenes from Dharwar peridotites agree well with the relative decrease in H observed in clinopyroxenes from Okidogo relative to Ichinomegata. Furthermore, based on REE concentrations of calculated hypothetical melts composition in equilibrium with Dharwar garnet (Pattnaik et al., 2020) and following the protocol of Aulbach et al. (2013), the results suggested that the metasomatic agent of the Dharwar cratonic lithospheric mantle is likely to be small volumes of carbonated silicate melt (Pattnaik et al., 2020), closely similar in composition to the natural kimberlite and lamproites from the Dharwar craton (e.g., Chalapathi Rao et al., 2013). This conclusion is further supported by the occurrence of kimberlite-carbonatite rocks in the Eastern Dharwar craton (Chatterjee et al., 2008; Smith et al., 2013), notably at the Khaderpet pipe, which is located only 15 km east of the Wajrakarur pipes. Thus, as recall above (section 4.1), if the metasomatic agent was CO_2-rich melt, it could have lowered the water fugacity in the system and could limit H incorporation in the NAMs lattice (e.g., Dixon and Stolper, 1995; Baptiste et al., 2015). Nonetheless, to strengthen this outcome, specific H partition coefficients between peridotitic minerals co-existing with the carbonated silicate melt would be necessary. To date, such experimental data are not yet available and only experiments with variable water activity are reported in simplified systems (e.g., Matveev et al., 2001, Wang et al., 2014, Gaetani et al., 2014, Tollan et al., 2018). Thus, further studies at high pressures are required to understand the partitioning of H in these complex petrological systems.

NAMs inclusions in diamonds prior to kimberlite emplacement are shielded from interaction with passing fluids and melts, which define the variation of H concentration in the

upper mantle and transition zone at the time of diamond formation, (e.g., Novella et al., 2015). Assuming that hydrogen diffusivity in diamond is indeed very slow (e.g., Popovici et al., 1995), we can thus consider these specimens are reliable H concentration proxy for the pristine mantle, that isolated NAMs from subsequent modification by discrete partial melting, melt-rock interactions, metasomatism or aqueous fluids percolation occurring within subcontinental mantle. A few studies reported H concentrations in inclusions in diamonds, using FTIR or secondary ion mass spectrometry (Kurosawa, 1997, Matsyuk and Langer, 2004, Novella, et al., 2015; Taylor et al., 2016, Jean et al., 2016), with striking lower H concentrations in olivine (0-34 ppm wt H_2O) when compared to co-existing olivines in cratonic peridotite xenoliths (Fig. 9). Nevertheless, rigorous comparisons remain challenging due to the paucity of accurate determination of equilibrium temperatures and pressures for these rare NAMs inclusions in diamonds.

4.4. Implication for the Dharwar Craton Viscosity

Incorporation of H in mantle minerals is recurrently proposed as a key parameter affecting many physical and chemical properties of the upper mantle minerals and rocks (e.g., Regenauer-Lieb and Kohl, 2003; Regenauer-Lieb et al., 2006; Albarède, 2009; Peslier et al. 2010; Demouchy and Bolfan-Casanova, 2016; Masuti et al., 2016). One particular property is the viscosity of olivine-rich rocks, which constitute about 67 vol.% of the lithospheric upper mantle (Demouchy and Bolfan-Casanova, 2016). It includes the lithosphere-asthenosphere boundary where a significant decrease in viscosity (from 10^{24} to 10^{20} Pa.s, e.g., Garel et al., 2014, 2020) is at the origin of partial mechanical decoupling, leading to the formation of a horizontal boundary of tectonic plates. Several studies have proposed that this partial mechanical decoupling between the lithosphere and asthenosphere is enhanced or even

triggered by H incorporation in olivine (Regenauer-Lieb and Kohl, 2003; Regenauer-Lieb et al., 2006, Peslier et al., 2010; Faul et al., 2016; Masuti et al., 2016). Combined with numerical modeling to test the longevity of South African cratonic root, it has been also proposed that a drastic decrease in H concentration in olivine at the base of a cratonic root would generate a 'hard shell', which protects the cratonic root from erosion by underlying convective asthenosphere (Peslier et al., 2010). Later on, this hypothesis was not confirmed by the results from the Siberian craton (Doucet et al., 2014). Furthermore, the most recent studies on H in olivine inclusions within diamond tend to confirm H depletion in cratonic root (Taylor et al., 2016; Jean et al., 2016) even if the depletion is not as drastic as reported previously (Kurosawa, 1997; Matsyuk and Langer, 2004; Novella et al., 2015).

Here, the mantle beneath the Dharwar craton is of particular interest to test this hypothesis because the Indian subcontinent was attached to Gondwana and located close to 40 °S-80 °E, before it drifted (~20 cm $year^{-1}$, e.g., Aitchinson et al., 2007) toward the Eurasian plate during Cretaceous, until collision began at Eocene (55 Ma, Aitchinson et al., 2007). Unfortunately, the results from rare Dharwar peridotitic olivines cannot permit to radically confirm or infirm the hypothetic marked H-depletion in olivine at the base of the cratonic root, since our mantle samples are not particularly from a deep upper mantle section (~5 GPa, i.e. < 150 km depth). Nevertheless, this is the first study which report the H concentrations in mantle minerals from the Indian cratonic mantle lithosphere and the results are in good agreements with the current data base for other mantle minerals and peridotites for similar depth. This value permits to calculate for the first time the viscosity of the Dharwar craton as a function of the hydrogen concentration. We can not use the most recent experimental study on hydroxyl weakening for dislocation glide and climb flow laws, that is equations (16) and (17) in Tielke et al., 2017, since these equations are not a function of the hydrogen concentration but use a fixed hydrogen concentration (60 $H/10^6Si$, which equals 3.7 ppm wt H_2O following the

582 calibration of Paterson, 1982). Nevertheless, we can use the dislocation creep flow laws given
583 by Hirth and Kohlstedt (2003, see their Table 1). We calculate the stress for a strain rate of $1 \times$
584 10^{-14} ms^{-1}, a temperature of 1179 °C (P3/6/3, T_{TA} reported in Table 1), a confining pressure of
585 5 GPa (P3/6/3, P_{NG} reported in Table 1), and the olivine hydrogen concentration of 11 ppm wt
586 H_2O (Table 3, thus equals to 178 $H/10^6Si$, with the calibration of Paterson, 1982). The ratio
587 stress/strain rate gives the viscosity, which yields 5.3×10^{20} Pa s for an anhydrous olivine and
588 1.5×10^{20} Pa s for hydrous olivine. The weakening factor is only 3.5 at high equilibrium
589 temperature and pressure of these xenoliths. Note that for a millimetric grain size, and a volume
590 fraction of olivine > 60%, the strength of a peridotite is not expected to be strongly impacted
591 by secondary phases (e.g., Ji et al., 2001). Therefore, we conclude that the occurrence of
592 hydrogen in olivine is not inducing a major change in viscosity of the Indian craton for these
593 conditions (hydrogen concentrations, high temperature and 165 km of depth).
594

595 **5. Conclusion**

596 We quantified the H concentrations in the four main rock-forming nominally anhydrous
597 minerals from a rare selection of peridotite xenoliths and minerals embedded in Wajrakarur
598 kimberlites from the Eastern Dharwar craton, India. We have demonstrated that olivines,
599 orthopyroxenes, clinopyroxenes and garnets from the Dharwar craton are of mantle origin. The
600 Dharwar peridotites show a range of H concentrations from 11-29 ppm wt H_2O in olivines,
601 from 56- 88 ppm wt H_2O in opx, from 81-642 ppm wt H_2O in cpx, and 14-15 ppm wt H_2O. in
602 garnets (using mineral-dependent calibration and excluding abnormal spectra). The range of H
603 concentrations in nominally anhydrous minerals present in Dharwar peridotites agrees well with
604 the current database for mantle minerals transported by kimberlites in other Archean cratons
605 (e.g., South Africa, Siberia) and are not especially indicative of a H-rich mantle lithosphere
606 beneath the Dharwar craton in the late Archean. Finally, despite having a limited number of

607 studied mantle samples, we provide the first estimate of bulk H concentration in mantle
608 minerals from the Dharwar craton. Our results also permit to quantify the negligible impact of
609 hydrogen on the viscosity of the Indian cratonic mantle.
610
611 **6. Acknowledgments**
612 S.D. thanks IIT KGP and the Dept. of Geology and Geophysics for financially
613 supporting her visit in November 2019 and for their remarkable welcome. S.D. thanks D.
614 Maurin for management of the FTIR lab at IRRAMAN platform of University of Montpellier
615 (France). S. G. thanks both ISIRD from IIT Kharagpur and the SERB-DST (grant no.
616 ERC/2015/000558) for financial support. J.P. acknowledges MHRD, Govt. of India for
617 supporting his Ph.D. fellowship. EPMA and LA-ICP-MS analyses were performed at the Dept.
618 Geology and Geophysics (IIT Kharagpur, India) with the help of S. Sinha and S. Ranjan,
619 respectively. The authors thank K. Tiwari for his help for producing Fig. 2d and deeply thank
620 Prof. J. Ganguly for the donation of very rare rocks and minerals from Wajrakarur kimberlite
621 field, India. We are also grateful to Prof. V. Pease for editorial comments and handling, and
622 two anonymous reviewers for constructive reviews.
623
624 **7. References**

625 Aitchison, J.C., Ali, J.R., Davis, A.M., 2007. When and where did India and Asia collide? J. Geophys.
626 Res. 112, 87–19. doi:10.1029/2006JB004706
627 Albarède, F., 2009. Volatile accretion history of the terrestrial planets and dynamic implications. Nature
628 461, 1227–1233. doi:10.1038/nature08477
629 Arai, S., 1994. Characterization of spinel peridotites by olivine-spinel compositional relationships:
630 review and interpretations. Chem. Geol. 113, 191-204.
631 Aulbach, S., Griffin, W.L., Pearson, N.J., O'Reilly, S.Y., 2013. Nature and timing of metasomatism in
632 the stratified mantle lithosphere beneath the central Slave craton (Canada). Chem. Geol., 352,
633 pp.153-169.
634 Bali, E., Bolfan-Casanova, N., Koga, K., 2008. Pressure and temperature dependence of H solubility in
635 forsterite: an implication to water activity in the Earth interior. Earth Planet. Sci. Lett. 268, 354–
636 363.

637 Baptiste, V., Demouchy, S., Keshav, S., Parat, F., Bolfan-Casanova, N., Condamine, P., Cordier, P.,
638 2015. Decrease of hydrogen incorporation in forsterite from CO_2-H_2O-rich kimberlitic liquid.
639 Am. Min. 100, 1912–1920. doi:10.2138/am-2015-5200
640 Baptiste, V., Tommasi, A., Demouchy, S., 2012. Deformation, hydration and seismic properties of the
641 lithospheric mantle beneath the Kaapval craton. Lithos 149, 31–50.
642 Bell, D.R., Gregoire, M., Grove, T.L., Chatterjee, N., Carlson, R.W., Buseck, P.R., 2005. Silica and
643 volatile-element metasomatism of Archean mantle: a xenolith-scale example from the Kaapvaal
644 Craton. Contrib. Mineral. Petrol. 150(3), 251-267 doi:10.1007/s00410-005-0673-8
645 Bell, D.R., Ihinger, P.D., Rossman, G.R., 1995. Quantitative and analysis of trace OH in garnet and
646 pyroxenes. Am. Min. 80, 465–474.
647 Bell, D.R., and Rossman, G.R., 1992a. Water in Earth's mantle: The role of nominally anhydrous
648 minerals. Science 255, 1391–1397.
649 Bell, D.R., and Rossman, G.R., 1992b. The distribution of hydroxyl in garnets from the subcontinental
650 mantle of southern Africa. Contrib. Mineral. Petrol. 111, 161-178.
651 Bell, D.R., Rossman, G.R., Maldener, J., Endisch, D., Rauch, F., 2003. Hydroxide in olivine: a
652 quantitative determination of the absolute amount and calibration of the IR spectrum. J. Geophys.
653 Res. 108 (B2). doi.org/10.1029/2001JB000679
654 Bell, D.R., Rossman, G.R., Moore, R.O., 2004. Abundance and partitioning of OH in a high-pressure
655 magmatic system: Megacrysts from the Monastery kimberlite, South Africa. J. Petrol. 45, 1539–
656 1564.
657 Beran, A., and Libowitzky, E. 2006. Water in natural mantle minerals II: Olivine, garnet and accessory
658 minerals. in: Keppler, H., Smyth, J.R., Rosso, J.J. (Eds.), Water in nominally anhydrous minerals.
659 American Mineralogical Society Geochemical Society, Chantilly (Vir.), Reviews in Mineralogy
660 and Geochemistry 62, 169–191. doi:10.2138/rmg.2006.62.8
661 Beran, A., and Zemman, J., 1969. Üder OH-gruppen in Olivin. Öster. Akad. Wiss. 3, 73–74.
662 Berry, A., Hermann, J., O'Neill, H.S.C., Foran, G.J., 2005. Fringerprinting the water site in mantle
663 olivine. Geology 33, 869–872.
664 Brey, G.P., and Köhler, T., 1990. Geothermobarometery in four-phase lherzolith II. New
665 thermobarometrers, and practical assessment of existing thremobarometers. J. Petrol. 31, 1353–
666 1378.
667 Carpenter Woods, S., Mackwell, S.J., Dyar, D., 2000. Hydrogen in diopside: Diffusion profiles. Am.
668 Min. 85, 480–487.
669 Chadwick, B., Vasudev, V.N. and Hegde, G. V., 2000. The Dharwar craton, southern India, interpreted
670 as the result of Late Archean oblique convergence. Precam. Res. 99, 91-111.
671 Chalapathi Rao, N.V., Wu, F.Y., Mitchell, R.H., Li, Q.L., Lehmann, B., 2013. Mesoproterozoic U-Pb
672 ages, trace element and Sr-Nd isotopic composition of perovskite from kimberlites of the
673 Eastern Dharwar craton, southern India: Distinct mantle sources and a widespread 1.1 Ga
674 tectonomagmatic event. Chem. Geol. 353, 48–64. doi.org/10.1016/j.chemgeo.2012.04.023.
675 Chalapathi Rao, N.V., Kumar, A., Sahoo, S., Dongre, A.N., Talukdar, D., 2014. Petrology and
676 petrogenesis of Mesoproterozoic lamproites from the Ramadugu field, NW margin of the
677 Cuddapah basin, Eastern Dharwar craton, southern India. Lithos 196-197, 150–168.
678 doi:10.1016/j.lithos.2014.03.007
679 Chatterjee, B., Haggerty, S.E., Beard, A., Smith, C.B., Townend, R., 2008. Kimberlite-carbonatite
680 relationship revisited: Evidence from Khaderpet pipe, Andhra Pradesh, India. International
681 Kimberlite Conference, Abstract #9IKC-A- 00070.
682 Costa, F., and Chakraborty, S., 2008. The effect of water in Si and O diffusion rates in olivine and
683 implications for the transport properties and processes in the upper mantle. Phys. Earth Planet.
684 Int. 166, 11–29.

De Hoog, J.C.M., Hattori, K., Jung, H., 2014. Titanium- and water-rich metamorphic olivine in high-pressure serpentinites from the Voltri Massif (Ligurian Alps, Italy): Evidence for deep subduction of high-field strength and fluid-mobile elements. Contrib. Mineral. Petrol. 167, 990. doi:10.1007/s00410-014-0990-x

Demouchy, S., and Bolfan-Casanova, N., 2016. Distribution and transport of hydrogen in the lithospheric mantle: A review. Lithos 240-243, 402–425. doi:10.1016/j.lithos.2015.11.012.

Demouchy, S., Ishikawa, A., Tommasi, A., Alard, O., Keshav, S., 2015. Characterization of hydration in the mantle lithosphere: Peridotite xenoliths from the Ontong Java Plateau as an example. Lithos 212-215, 189–201. doi:10.1016/j.lithos.2014.11.005.

Demouchy, S., and Mackwell, S.J., 2003. Water diffusion in synthetic iron-free forsterite. Phys. Chem. Mineral. 30, 486–494.

Demouchy, S., and Mackwell, S.J., 2006. Mechanisms of hydrogen incorporation and diffusion in iron-bearing olivine. Phys. Chem. Mineral. 33, 347–355.

Demouchy, S., Mackwell, S.J., Kohlstedt, D.L., 2007. Influence of hydrogen on Fe–Mg interdiffusion in (Mg,Fe)O and implications for Earth's lower mantle. Contrib. Mineral. Petrol. 154, 279–289.

Demouchy, S., Shcheka, S., Denis, C.M.M., Thoraval, C., 2017. Subsolidus hydrogen partitioning between nominally anhydrous minerals in garnet-bearing peridotite. Am. Min. 102, 1822–1831. doi:10.2138/am-2017-6089.

Demouchy, S., Tommasi, A., Barou, F., Mainprice, D., Cordier, P., 2012. Deformation of olivine in torsion under hydrous conditions. Phys. Earth Planet. Int. 202-203, 57–70. doi:10.1029/2008GL036611

Demouchy, S., Tommasi, A., Ionov, D., Higgie, K., Carlson, R.W., 2019. Microstructures, water contents, and seismic properties of the mantle lithosphere beneath the northern limit of the Hangay Dome, Mongolia. Geochem. Geophys. Geosys. 2018GC007931. doi:10.1029/2018GC007931

Denis, C.M.M., Alard, O., Demouchy, S., 2015. Water content and hydrogen behaviour during metasomatism in the uppermost mantle beneath Ray Pic volcano (Massif Central, France). Lithos 236-237, 256–274. doi:10.1016/j.lithos.2015.08.013

Denis, C.M.M., Demouchy, S., Alard, O., 2018. Heterogeneous hydrogen distribution in orthopyroxene from veined mantle peridotite (San Carlos, Arizona): Impact of melt-rock interactions. Lithos 302-303, 298–311. doi:10.1016/j.lithos.2018.01.007.

Denis, C.M.M., Demouchy, S., Shaw, C., 2013. Evidence of dehydration in peridotites from Eifel Volcanic Field and estimates of magma ascent rates. J. Volc. Geoth. Res. 258, 85–99.

Dick, H.J., and Bullen, T., 1984. Chromian spinel as a petrogenetic indicator in abyssal and alpine-type peridotites and spatially associated lavas. Contrib. Mineral. Petrol. 86(1), 54-76.

Dixon, J.E., Leist, L., Langmuir, C., Schilling, J.-G., 2002. Recycled dehydrated lithosphere observed in plume-influenced mid-ocean ridge-basalt. Nature 420, 385–389.

Dixon, J.E., and Stolper, E.M., 1995. An experimental study of water and carbon dioxide solubilities in mid-ocean ridge basaltic liquids. Part II: applications to degassing. J. Petrol. 36(6), 1633-1646.

Dongre, A.N., Jacob, D.E., Stern, R.A., 2015. Subduction-related origin of eclogite xenoliths from the Wajrakarur kimberlite field, Eastern Dharwar craton, Southern India: Constraints from petrology and geochemistry. Geochim. Cosmochim. Acta 166, 165–188. doi:10.1016/j.gca.2015.06.023

Doucet, L.S., Ionov, D.A., Golovin, A.V., Pokhilenko, N.P., 2012. Depth, degrees and tectonic settings of mantle melting during craton formation inferences from major and trace element compositions of spinel harzburgite xenoliths from the Udachnaya kimberlite, central Siberia. Earth Planet. Sci. Lett 359-360, 206–218. doi:10.1016/j.epsl.2012.10.001

Doucet, L.S., Peslier, A.H., Ionov, D.A., Brandon, A.D., Golovin, A.V., Goncharov, A.G., Ashchepkov, I.V., 2014. High water contents in the Siberian cratonic mantle linked to metasomatism: an FTIR

study of Udachnaya peridotite xenoliths. Geochim. Cosmochim. Acta 137, 159-187. doi:10.1016/j.gca.2014.04.011

Fareeduddin and Mitchell, R.H., (2012) Diamond and their source rocks in India. Geological Society of India, Bangalore, 434 pp.

Faul, U.H., Cline, C.J., II, David, E.C., Berry, A.J., Jackson, I., 2016. Titanium-hydroxyl defect-controlled rheology of the Earth's upper mantle. Earth Planet. Sci. Lett. 452, 227–237. doi:10.1016/j.epsl.2016.07.016

Fei, H., and Katsura, T., 2020. Pressure dependence of proton incorporation and water solubility in olivine. J. Geophys. Res. 125, 83–13. doi:10.1029/2019JB018813

Férot, A., Bolfan-Casanova, N., 2012. Water storage capacity in olivine and pyroxene to 14 GPa: Implications for the water content of the Earth's upper mantle and nature of seismic discontinuities. Earth Planet. Sci. Lett. 349-350, 218–230.

Ferriss, E., Plank, T., Walker, D., 2016. Site-specific hydrogen diffusion rates during clinopyroxene dehydration. Contrib. Mineral. Petrol. 171(6), 1–24. doi:10.1007/s00410-016-1262-8

Gaetani, G.A., Grove, T.L., 1998. The influence of water on melting of mantle peridotite. Contrib. Mineral. Petrol. 131, 323–346.

Gaetani, G.A., O'Leary, J.A., Koga, K.T., Hauri, E.H., Rose-Koga, E.F., Monteleone, B.D., 2014. Hydration of mantle olivine under variable water and oxygen fugacity conditions. Contrib. Mineral. Petrol. 167, 965. doi:10.1007/s00410-014-0965-y

Ganguly, J., and Bhattacharya, P.K., 1987. Xenoliths in Proterozoic kimberlites from southern India: Petrology and geophysical implications. In: Mantle Xenoliths, Nixon, P.H. (Ed.) John Wiley and Sons Ltd. John Wiley, New York, pp 249-266.

Garel, F., Goes, S., Davies, D.R., Davies, J.H., Kramer, S.C., Wilson, C.R., 2014. Interaction of subducted slabs with the mantle transition-zone: A regime diagram from 2-D thermo-mechanical models with a mobile trench and an overriding plate. Geochem. Geophys. Geosys. 15, 1739–1765. doi:10.1002/2014GC005257

Garel, F., Thoraval, C., Tommasi, A., Demouchy, S., Davies, D.R., 2020. Using thermo-mechanical models of subduction to constrain effective mantle viscosity. Earth Planet. Sci. Lett. 539, 116243. doi:10.1016/j.epsl.2020.116243.

Geiger, C.A., and Rossman, G.R., 2018. IR spectroscopy and OH– in silicate garnet: The long quest to document the hydrogarnet substitution. Am. Min. 103, 384–393. doi:10.2138/am-2018-6160CCBY

Gibson, S.A., Malarkey, J. Day, J.A., 2008. Melt depletion and enrichment beneath the western Kaapvaal Craton: evidence from Finsch peridotite xenoliths. J. Petrol. 49(10), 1817-1852.

Gopalan, K., and Kumar, A., 2008 Phlogopite K-Ca dating of Narayanpet kimberlites, South India: Implications to the discordance between their Rb-Sr, Ar/Ar ages. Precam. Res. 167, 377-382.

Grant, K., Ingrin, J., Lorand, J.P., Dumas, P., 2007. Water partitioning between mantle minerals from peridotite xenoliths. Contrib. Mineral. Petrol. 154, 15–34.

Grégoire, M., Tinguely, C., Bell, D.R., Le Roex, A.P., 2005. Spinel lherzolite xenoliths from the Premier kimberlite (Kaapvaal craton, South Africa): nature and evolution of the shallow upper mantle beneath the Bushveld complex. Lithos 84(3-4), 185-205.

Hanger, B.J., Yaxley, G.M., Berry, A.J. and Kamenetsky, V.S., 2015. Relationships between oxygen fugacity and metasomatism in the Kaapvaal subcratonic mantle, represented by garnet peridotite xenoliths in the Wesselton kimberlite, South Africa. Lithos 212, 443-452.

Hills, D.V. and Haggerty, S.E., 1989. Petrochemistry of eclogites from the Koidu kimberlite complex, Sierra Leone. Contrib. Mineral. Petrol. 103(4), 397-422.

778 Hirschmann, M.M., Tenner, T., Aubaud, C., Withers, A.C., 2009. Dehydration melting of nominally
779 anhydrous mantle: The primacy of partitioning. Phys. Earth Planet. Int. 176, 54–68.
780 doi:10.1016/j.pepi.2009.04.001
781 Hirth, G., and Kohlstedt, D.L., 1996. Water in the oceanic upper mantle: implications for rheology, melt
782 extraction and the evolution of the lithosphere. Earth Planet. Sci. Lett. 144, 93–108.
783 Hirth, G., and Kohlstedt, D.L., 2003. Rheology of the upper mantle and the mantle wedge: A view from
784 the experimentalists, in: Eiler, J. (Ed.), Inside The Subduction Factory. American Geophysical
785 Union, Washington D.C., pp. 83–105.
786 Ingrin, J., and Skogby, H., 2000. Hydrogen in nominally anhydrous upper-mantle minerals:
787 concentration levels and implications. Eur. J. Mineral. 12, 543–570.
788 Ionov, D.A., Doucet, L.S., Ashchepkov, I.V., 2010. Composition of the lithospheric mantle in the
789 Siberian craton: new constraints from fresh peridotites in the Udachnaya-East kimberlite. J.
790 Petrol. 51(11), 2177-2210.
791 Jayananda, M., Santosh, M., Aadhiseshan, K.R., 2018. Formation of Archean (3600–2500 Ma)
792 continental crust in the Dharwar Craton, southern India. Earth Sci. Rev.181, 12–42.
793 Jean, M.M., Taylor, L.A., Howarth, G.H., Peslier, A.H., Fedele, L., Bodnar, R.J., Guan, Y., Doucet,
794 L.S., Ionov, D.A., Logvinova, A.M., Golovin, A.V., Sobolev, N.V., 2016. Olivine inclusions in
795 Siberian diamonds and mantle xenoliths: Contrasting water and trace-element contents. Lithos
796 265, 31–41. doi:10.1016/j.lithos.2016.07.023.
797 Jerde, E.A., Taylor, L.A., Crozaz, G., Sobolev, N.V., Sobolev, V.N., 1993. Diamondiferous eclogites
798 from Yakutia, Siberia: Evidence for a diversity of protoliths. Contrib. Mineral. Petrol. 114(2),
799 189-202.
800 Ji, S., Wang, Z., Wirth, R., 2001. Bulk flow strength of forsterite-enstatite composites as a function of
801 forsterite content. Tectonophysics 341, 69–93.
802 Kamenetsky, V.S., Kamenetsky, M.B., Sobole, A.V., Golovin, A.V., Demouchy, S., Faure, K.,
803 Sharygin, V.V., Kuzmin, D.V., 2008. Olivine in the Udachnaya-East Kimberlite (Yakutia,
804 Russia): Types, compositions and origins. J. Petrol. 49, 823–839.
805 Karato, S.I., 1990. The role of hydrogen diffusivity in the electrical conductivity of the upper mantle.
806 Nature 347, 272–273.
807 Karmalkar, N.R., Duraiswami, R.A., Rao, N.C., Paul, D.K., 2009. Mantle-derived mafic-ultramafic
808 xenoliths and the nature of Indian sub-continental lithosphere. J. Geol. Soc. India 73(5), 657.
809 Katayama, I., Nakashima, S., Yurimoto, H., 2006. Water content in natural eclogite and implication for
810 water transport into the deep upper mantle. Lithos 86, 245–259. doi:10.1016/j.lithos.2005.06.006.
811 Kent, A.J.R., Rossman, G.R., 2002. Hydrogen, lithium, and boron in mantle-derived olivine: the role of
812 coupled substitutions. Am. Min. 87, 1432–1436.
813 Keppler, H., and Bolfan-Casanova, N., 2006. Thermodynamics of Water Solubility and Partitioning, in:
814 Keppler, H., Smyth, J.R., Rosso, J.J. (Eds.), Water in Nominally Anhydrous Minerals. American
815 Mineralogical Society Geochemical Society, Chantilly (Vir.), pp. 193–230.
816 Koch-Mueller, M., Matsyuk, S.S., Rhede, D., Wirth, R., Khisina, N., 2006. Hydroxyl in mantle olivine
817 xenocrysts from the Udahnaya kimberlite pipe. Phys. Chem. Mineral. 33, 276–287.
818 Kohlstedt, D.L., Keppler, H., Rubie, D.C., 1996. Solubility of water in the α, β and γ–phases of
819 $(Mg,Fe)_2SiO_4$. Contrib. Mineral. Petrol. 123, 345–357.
820 Konzett, J., Wirth, R., Hauzenberger, C., Whitehouse, M., 2013. Two episodes of fluid migration in the
821 Kaapvaal Craton lithospheric mantle associated with Cretaceous kimberlite activity: evidence
822 from a harzburgite containing a unique assemblage of metasomatic zirconium-phases. Lithos 182,
823 165-184.

824 Kopylova, M.G., Russell, J.K., Cookenboo, H., 1999. Petrology of peridotite and pyroxenite xenoliths
825 from the Jericho kimberlite: implications for the thermal state of the mantle beneath the Slave
826 craton, northern Canada. J. Petrol. 40(1), 79-104.
827 Kovàcs, I., Hermann, J., O'Neill, H.S.C., Gerald, J.F., Sambridge, M., Horvàth, G., 2008. Quantitative
828 absorbance spectroscopy with unpolarized light: Part II. Experimental evaluation and
829 development of a protocol for quantitative analysis of mineral IR spectra. Am. Min. 93, 765–
830 778. doi:10.2138/am.2008.2656.
831 Kurosawa, M., Yurimoto, H., Sueno, S., 1997. Patterns in the hydrogen and trace element compositions
832 of mantle olivines. Phys. Chem. Mineral. 24, 385-395.
833 Lazarov, M., Woodland, A.B., Brey, G.P., 2009. Thermal state and redox conditions of the Kaapvaal
834 mantle: A study of xenoliths from the Finsch mine, South Africa. Lithos 112, 913-923.
835 Li, Z.X.A., Lee, C.T.A., Peslier, A., Lenardic, A., Mackwell, S.J., 2008. Water contents in mantle
836 xenoliths from the Colorado Plateau and vicinity: implications for the mantle rheology and
837 hydration-induced thining of continental lithosphere. J. Geophys. Res. 113, doi: 10.1029–
838 2007JB005540.
839 Litasov, K.D., Ohtani, E., Kagi, H., Jacobsen, S.D., Ghosh, S., 2007. Temperature dependence and
840 mechanism of hydrogen incorporation in olivine at 12.5-14.0 GPa. Geophys. Res. Lett. 34, 460–
841 5. doi:10.1029/2007GL030737
842 MacGregor, I.D. and Manton, W.I., 1986. Roberts Victor eclogites: ancient oceanic crust. J. Geophys.
843 Res. 91(B14), 14063-14079.
844 MacKenzie, J.M. and Canil, D., 1999. Composition and thermal evolution of cratonic mantle beneath
845 the central Archean Slave Province, NWT, Canada. Contrib. Mineral. Petrol. 134(4), 313-324.
846 Mackwell, S.J., and Kohlstedt, D.L., 1990. Diffusion of hydrogen in olivine: Implications for water in
847 the mantle. J. Geophys. Res. 95, 5079–5088.
848 Mackwell, S.J., Kohlstedt, D.L., Paterson, M.S., 1985. The role of water in the deformation of olivine
849 single crystals. J. Geophys. Res. 90, 11319-11333.
850 Maldener, J., Hösch, A., Langer, K., Rauch, F., 2003. Hydrogen in some natural garnets studied by
851 nuclear reaction analysis and vibrational spectroscopy. Phys. Chem. Mineral. 30, 337–344.
852 Marty, B., 2012. The origins and concentrations of water, carbon, nitrogen and noble gases on Earth.
853 Earth Planet. Sci. Lett. 313-314, 56–66. doi:10.1016/j.epsl.2011.10.040
854 Masuti, S., Karato, S.-I., Feng, L., Banerjee, P., Barbot, S.D., 2016. Upper-mantle water stratification
855 inferred from observations of the 2012 Indian Ocean earthquake. Nature 538, 373–377.
856 doi:10.1038/nature19783.
857 Matsyuk, S.S., and Langer, K., 2004. Hydroxyl in olivines from mantles xenoliths in kimberlites of the
858 Siberian platform. Contrib. Mineral. Petrol. 147, 413–437.
859 Matsyuk, S.S., Langer, K., Hoesch, A., 1998. Hydroxyl defects in garnet from mantle xenoliths in
860 kimbelites of the Siberian platform. Contrib. Mineral. Petrol. 132, 163–179.
861 Matveev, S., O'Neill, H.S.C., Ballhaus, C., Taylor, W.R., Green, D.H., 2001. Effect of silica activity on
862 OH−IR spectra of olivine: implications for low-a SiO_2 mantle metasomatism. J. Petrol. 42(4),
863 721-729.
864 Menzies, A., Westerlund, K., Grütter, H., Gurney, J., Carlson, J., Fung, A., Nowicki, T., 2004.
865 Peridotitic mantle xenoliths from kimberlites on the Ekati Diamond Mine property, NWT,
866 Canada: major element compositions and implications for the lithosphere beneath the central
867 Slave craton. Lithos, 77(1-4), 395-412.
868 Michael, P.J., 1988, The concentration, behaviour and storage of H_2O in the suboceanic upper mantle:
869 Implication for mantle metasomatism. Geochimi. Cosmochim. Acta 52, 555-566.
870 Mierdel, K., and Keppler, H., 2004. The temperature dependence of water solubility in enstatite. Contrib.
871 Mineral. Petrol. 148, 305–311.

872 Mierdel, K., Keppler, H., Smyth, J.R., Langerhorst, F., 2007. Water solubility in aluminous
873 orthopyroxene and the origin of the asthenosphere. Science 315, 364–368.
874 Miller, G.H., Rossman, G.R., Harlow, G.E., 1987. The natural occurrence of hydroxide in olivine. Phys.
875 Chem. Mineral. 14, 461–472.
876 Mookherjee, M., and Karato, S.-I., 2010. Solubility of water in pyrope-rich garnet at high pressures and
877 temperature. Geophys. Res. Lett. 37, L03310. doi:10.1029/2009GL041289
878 Nakamura, A., and Schmalzried, H., 1983. On the nonstoichiometry and point defects of olivine. Phys.
879 Chem. Mineral. 10, 27–37.
880 Naqvi, S.M., and Rogers, J.J.W., 1987 Precambrian Geology of India, Oxford University Press, New
881 York, 223.
882 Nayak, S.S., and Kudari, S.A.D., 1999. Discovery of diamond-bearing kimberlites in Kalyandurg area,
883 Anantapur district, Andhra Pradesh. Current Science, 76(8), 1077-1079.
884 Neelkantam, S., 2001. Exploration for diamond in southern India. Geological Survey of India Special
885 Publication 58, 521-555.
886 Nehru, C.E., and Reddy, A.K., 1989. Ultramafic xenoliths from Vajrakarur kimberlites, India.
887 Geolological Society of Australia Special Publication, 14, 745-758.
888 Nickel, K.G. and Green, D.H., 1985. Empirical geothermobarometry for garnet peridotites and
889 implications for the nature of the lithosphere, kimberlites and diamonds. Earth Planet. Sci.
890 Lett. 73(1), 158-170.
891 Nimis, P., and Grütter, H., 2010. Internally consistent geothermometers for garnet peridotites and
892 pyroxenites. Contrib. Mineral. Petrol. 159(3), 411-427.
893 Novella, D., Bolfan-Casanova, N., Nestola, F., Harris, J.W., 2015. H_2O in olivine and garnet inclusions
894 still trapped in diamonds from the Siberian craton: Implications for the water content of cratonic
895 lithosphere peridotites. Lithos 230, 180–183. doi:10.1016/j.lithos.2015.05.013.
896 Novella, D., Frost, D.J., Hauri, E.H., Bureau, H., Raepsaet, C., Roberge, M., 2014. The distribution of
897 H_2O between silicate melt and nominally anhydrous peridotite and the onset of hydrous melting
898 in the deep upper mantle. Earth Planet. Sci. Lett. 400, 1–13. doi:10.1016/j.epsl.2014.05.006
899 Novella, D., Jacobsen, B., Weber, P.K., Tyburczy, J.A., Ryerson, F.J., Frane, Du, W.L., 2017. Hydrogen
900 self-diffusion in single crystal olivine and electrical conductivity of the Earth's mantle. Scientific
901 Report 7, 629. doi:10.1038/s41598-017-05113-6.
902 O'Leary, J.A., Gaetani, G.A., Hauri, E.H., 2010. The effect of tetrahedral Al3+ on the partitioning of
903 water between clinopyroxene and silicate melt. Earth Planet. Sci. Lett. 297, 111–120.
904 doi:10.1016/j.epsl.2010.06.011.
905 O'Reilly, S.Y., Chen, D., Griffin, W.L., Ryan, C.G., 1997. Minor elements in olivine from spinel
906 lherzolite xenoliths: Implication for thermobarometry. Min. Mag. 61, 257-269.
907 Osborne, I., Sherlock, S., Anand, L., Argles, T., 2011. New Ar-Ar ages of southern Indian kimberlites
908 and lamphroite and their geochemical evolution. Precam. Res.189/ 91-103.
909 Padrón-Navarta, J.A., and Hermann, J., 2017. A subsolidus olivine water solubility equation for the
910 Earth's upper mantle. J. Geophys. Res. 122, 9862–9880. doi:10.1002/2017JB014510.
911 Padrón-Navarta, J.A., Hermann, J., O'Neill, H.S.C., 2014. Site-specific hydrogen diffusion rates in
912 forsterite. Earth Planet. Sci. Lett. 392, 100–112. doi: 10.1016/j.epsl.2014.01.055
913 Patel, S.C., Ravi, S., Anilkumar, Y., Naik, A., Thakur, S.S., Pati, J.K. and Nayak, S.S., 2009. Mafic
914 xenoliths in Proterozoic kimberlites from Eastern Dharwar Craton, India: mineralogy and P–T
915 regime. J. Asian Earth Sci., 34(3), 336-346. doi: 10.1016/j.jseaes.2008.06.001
916 Paterson, M.S., 1982. The determination of hydroxyl by infrared absorption in quartz, silicate glasses
917 and similar materials. Bulle. Min. 105, 20–29.
918 Pattnaik, J., Ghosh, S., Dongre, A., 2020. Plume activity and carbonated silicate melt metasomatism in
919 ancient lithospheric mantle beneath the Eastern Dharwar Craton: Evidence from petrology and

920 geochemistry of peridotite xenoliths in Wajrakarur kimberlites, Lithos, doi:10.1016/j.lithos.
921 2020.105726.
922 Pearson, D.G., Woodhead, J., Janney, P.E., 2019. Kimberlites as geochemical probes of Earth's
923 mantle. Elements, 15(6), 387-392.
924 Peslier, A.H., 2010. A review of water contents of nominally anhydrous minerals in the mantles of Earth,
925 Mars and the Moon. J. Volc. Geoth. Res. 197, 239–258.
926 Peslier, A.H., Luhr, J., Post, J., 2002. Low water contents in pyroxenes from spinel-peridotites of the
927 oxidized, sub-arc mantle wedge. Earth Planet. Sci. Lett. 201, 69–86.
928 Peslier, A.H., Woodland, A.B., Bell, D.R., Lazarov, M., 2010. Olivine water contents in the continental
929 lithosphere and the longevity of cratons. Nature 467, 78–83.
930 Peslier, A.H., Woodland, A.B., Bell, D.R., Lazarote, M., Lapen, T.J., 2012. Metasomatic control of
931 water contents in the kaapvaal cratonic mantle. Geochim. Cosmochim. Acta 97, 213–246.
932 Peslier, A. H., Woodland, A.B., Wolff, J.A., 2008. Fast kimberlite ascent rate estimates from hydrogen
933 diffusion profiles in xenoliths mantle olivines from South Africa. Geochim. Cosmochim. Acta.
934 72, 2711–2722.
935 Poe, B.T., Romano, C., Nestola, F., Smyth, J.R., 2010. Electrical conductivity anisotropy of dry and
936 hydrous olivine at 8 GPa. Phys. Earth Planet. Int. 181, 103–111. doi:10.1016/j.pepi.2010.05.003
937 Popovici, G., Wilson, R.G., Sung, T., Prelas, M.A., Khasawinah, S., 1995. Diffusion of boron, lithium,
938 oxygen, hydrogen, and nitrogen in type IIa natural diamond. J. Appl. Phys. 77, 5103–5106.
939 Post, J.L., and Borer, L., 2000. High-resolution infrared spectra, physical properties, and
940 micromorphology of serpentines. Appl. Clay Sci.16, 73–85.
941 Ramakrishnan, M., and Vaidyanadhan, R. 2010. Geology of India, Vol 1., Second Ed. Geological
942 Society of India, Bangalore.
943 Rauch, M., 2000. Der Einbau von Wasser in Pyroxene, PhD thesis, Bayerisches Geoinstitut. Bayreuth
944 Universität, Bayreuth.
945 Ravi, S., Sufija, M.V., Patel, S.C., Sheikh, J.M., Sridhar, M., Kaminsky, F.V., Khachatryan, G.K.,
946 Nayak, S.S., Bhaskara Rao, K.S., 2013. Diamond Potential of the Eastern Dharwar Craton,
947 Southern India, and a Reconnaissance Study of Physical and Infrared Characteristics of the
948 Diamonds, in: Proceedings of 10th International Kimberlite Conference. Springer India, New
949 Delhi, 335–348. doi:10.1007/978-81-322-1170-9_23
950 Ravi, S., Vaideswaran, T., Rao, K.S.B., 2009. Field guide to Wajrakarur kimberlite field, Anantpur
951 district, Andhra Pradesh. Geological Survey of India, 1-43.
952 Regenauer-Lieb, K., and Kohl, T., 2003. Water solubility and diffusivity in olivine: its role in planetary
953 tectonics. Min. Mag. 67(4), 697–715.
954 Regenauer-Lieb, K., Weinberg, R.F., Rosenbaum, G., 2006. The effect of energy feedbacks on
955 continental strength. Nature 442, 67–70.
956 Rossman, G.R., and Aines, R.D., 1991. The hydrous components in garnet: Grossular-hydrogrossular.
957 Am. Min. 76, 1153-1164.
958 Saal, A.E., Hauri, E.H., Langmuir, C.H., Perfit M.R., 2002. Vapour undersaturation in primitive mid-
959 ocean-ridge basalt and the volatile content of Earth's upper mantle. Nature 419, 451–455.
960 Satsukawa, T., Godard, M., Demouchy, S., Michibayashi, K., Ildefonse, B., 2017. Chemical interactions
961 in the subduction factory: New insights from an *in situ* trace element and hydrogen study of the
962 Ichinomegata and Oki-Dogo mantle xenoliths (Japan). Geochim. Cosmochim. Acta 208, 234–
963 267. doi:10.1016/j.gca.2017.03.042
964 Schmädicke, E., Gose, J., Witt-Eickschen, G., Brätz, H., 2013. Olivine from spinel peridotite xenoliths:
965 Hydroxyl incorporation and mineral composition. Am. Min. 98, 1870–1880
966 Shaikh, A.M., Tappe, S., Bussweiler, Y., Patel, S.C., Ravi, S., Bolhar, R., Viljoen, F., 2020.
967 Clinopyroxene and garnet mantle cargo in kimberlites as probes of Dharwar craton architecture

and geotherms, with implications for post 1.1 GPa lithosphere thinning events beneath southern India. J. Petrol. doi: 10.1093/petrology/egaa087.
Sheng, Y.-M., Xia, Q.-K., Dallai, L., Yang, X.-Z., Hao, Y.-T., 2007. H_2O contents and D/H ratios of nominally anhydrous minerals from ultrahigh-pressure eclogites of the Dabie orogen, eastern China. Geochim. Cosmochim. Acta 71, 2079–2103. doi:10.1016/j.gca.2007.01.018
Skogby, H., 2006. Water in natural mantle minerals I: Pyroxenes, in: Keppler, H., Smyth, J.R., Rosso, J.J. (Eds.), Water in Nominally Anhydrous Minerals. American Mineralogical Society Geochemical Society, Chantilly (Vir.), vol. 62, pp. 155–167.
Skogby, H., Bell, D.R., Rossman, G.R. 1990. Hydroxide in pyroxene; variations in the natural environment. Am. Min.*75*(7-8), 764-774.
Skogby, H., Rossman, G.R., 1989. OH-in pyroxene: An experimental study of incorporation mechanisms and stability. Am. Min.74, 1059–1069.
Smith, C.B., Haggerty, S.E., Chatterjee, B., Beard, A., Townend, R., 2013. Kimberlite, lamproite, ultramafic lamprophyre, and carbonatite relationships on the Dharwar Craton, India: An example from the Khaderpet pipe, a diamondiferous ultramafic with associated carbonate intrusion, Lithos 183, 102-113.
Snyder, G.A., Taylor, L.A., Crozaz, G., Halliday, A.N., Beard, B.L., Sobolev, V.N. and Sobolev, N.V., 1997. The origins of Yakutian eclogite xenoliths. J. Petrol. 38(1), 85-113.
Sobolev, V.N., Taylor, L.A., Snyder, G.A., Sobolev, N.V., 1994. Diamondiferous eclogites from the Udachnaya kimberlite pipe, Yakutia. Inter. Geol. Rev. 36(1), 42-64.
Stalder, R., 2004. Influence of Fe, Cr, and Al on hydrogen incorporation in orthopyroxene. Eur. J. Mineral. 16, 703–711.
Stalder, R., Karimova, A., Konzett, J., 2015. OH-defects in multiple-doped orthoenstatite at 4-8 GPa: filling the gap between pure and natural systems. Contrib. Mineral. Petrol. 169, 38, doi:10.1007/s00410-015-1133-8
Stalder, R., Klemme, S., Ludwig, T., Skogby, H., 2005. Hydrogen incorporation in orthopyroxene: interaction of different trivalent cations. Contrib. Mineral. Petrol. 150, 473–485. doi:10.1007/s00410-005-0037-4
Stalder, R., and Ludwig, T., 2007. OH incorporation in synthetic diopside. Eur. J. Mineral. 19, 373–380.
Sun, W., Yoshino, T., Kuroda, M., Sakamoto, N., Yurimoto, H., 2019. H-D interdiffusion in single-crystal olivine: Implications for electrical conductivity in the upper mantle. J. Geophys. Res. 124 (56), 5696-5707.
Taylor, W.R., 1998. An experimental test of some geothermometer and geobaro meterformulations for upper mantle peridotites with application to the ther-mobarometry offertile lherzolite and garnet websterite. Neues Jahrbuch für Mineralogie-Abhandlungen 381–408.
Taylor, L.A., Logvinova, A.M., Howarth, G.H., Liu, Y., Peslier, A.H., Rossman, G.R., Guan, Y., Chen, Y., Sobolev, N.V., 2016. Low water contents in diamond mineral inclusions: Proto-genetic origin in a dry cratonic lithosphere. Earth Planet. Scie. Lett. 433, 125–132. doi:10.1016/j.epsl.2015.10.042.
Tenner, T.J., Hirschmann, M.M., Withers, A.C., Hervig, R.L., 2009. Hydrogen partitioning between nominally anhydrous upper mantle minerals and melt between 3 and 5 GPa and applications to hydrous peridotite partial melting. Chem. Geol. 262, 42–56. doi:10.1016/j.chemgeo.2008.12.006.
Tielke, J., A., Zimmerman, M.E, Kohlstedt, D.L., 2017. Hydrolytic weakening in olivine single crystals. J. Geophys. Res. 122(5), 3465-3479, doi:10.1002/(ISSN)2169-9356.
Thoraval, C., Demouchy, S., 2014. Numerical models of ionic diffusion in one and three dimensions: application to dehydration of mantle olivine. Phys. Chem. Mineral. 41, 709–723. doi:10.1007/s00269-014-0685-x

Thoraval, C., Demouchy, S., Padrón-Navarta, J.A., 2019. Relative diffusivities of hydrous defects from a partially dehydrated natural olivine. Phys. Chem. Mineral. 46, 1–13. doi:10.1007/s00269-018-0982-x

Tollan, P.M.E., O'Neill, H.St.C., Hermann, J., 2018. The role of trace elements in controlling H incorporation in San Carlos olivine. Contrib. Mineral. Petrol. 173, 89. doi:10.1007/s00410-018-1517-7

Tran, H., and Nguyen, H., 2018. Petrology, geochemistry, and Sr, Nd isotopes of mantle xenolith in Nghia Dan alkaline basalt (West Nghe An): implications for lithospheric mantle characteristics beneath the region. Vietnam J. Earth Sci. 40. 207-227. 10.15625/0866-7187/40/3/12614.

Walker, A.M., Hermann, J., Berry, A., O'Neill, H.S., 2007. Three water sites in the upper mantle olivine and the role of titanium in the water weakening mechanism. J. Geophys. Res. 112 (B5). doi:10.1029–2006JB004620.

Wang, Q., Bagdassarov, N., Xia, Q.K., Zhu, B., 2014. Water contents and electrical conductivity of peridotite xenoliths from the North China Craton: Implications for water distribution in the upper mantle. Lithos 189, 105-126.

Withers, A.C., Bureau, H., Raepsaet, C., Hirschmann, M.M., 2012. Calibration of infrared spectroscopy by elastic recoil detection analysis of H in synthetic olivine. Chem. Geol. 334, 92–98.

Withers, A.C., Wood, B.J., Carroll, M., 1998. The OH content of pyrope at high pressure. Chem. Geol. 147, 161–171.

Xia, Q.K., Sheng, Y.M., Yang, X.Z., Yu, H.M., 2005. Heterogeneity of water in garnets from UHP eclogites, eastern Dabieshan, China. Chem. Geol. 224, 237–246.

Yang, X.-Z., Xia, Q.-K., Deloule, E., Dallai, L., Fan, Q.-C., Feng, M., 2008. Water in minerals of the continental lithospheric mantle and overlying lower crust: A comparative study of peridotite and granulite xenoliths from the North China Craton. Chem. Geol. 256, 33–45. doi:10.1016/j.chemgeo.2008.07.020.

Yoshino, T., Matsuzaki, T., Yamashita, S., Katsura, T., 2006. Hydrous olivine unable to account for conductivity anomaly at the top of the asthenosphere. Nature 443(7114), 973–976.

Figures Captions

Figure 1. (a) Geological map of southern India comprising of different tectonic units redrawn from Patel et al. (2009). EDC: Eastern Dharwar Craton, WDC: Western Dharwar Craton, EGMB: Eastern Ghat Mobile Belt, CG: Closepet granite and equivalents, GG: Godavari graben, NKF: Narayanpet kimberlite field, RKF: Raichur kimberlite field, WKF: Wajrakarur kimberlite field, CBF: Chitradurga boundary fault. (b) Enlarged map of Wajrakarur kimberlite field showing locations of studied samples (after Nayak and Kudari, 1999).

Figure 2. Peridotite xenolith and mineral micrographs from Wajrakarur kimberlites field, Eastern Dharwar craton. (a) Thin section scans in natural light of spinel (± garnet) peridotite (sample P3/5/1) showing granular texture with highly fractured large olivine grains, elongated shaped orthopyroxenes, clinopyroxenes surrounding the olivines as veinlets. (b) Garnet peridotite (sample P3/6/1) with polygonal garnets in a matrix of orthopyroxenes and clinopyroxenes along with euhedral larger grains of olivines. (c) Sample P3/6/3 with mantle olivine xenocrysts present in the kimberlitic matrix. (d) Mantle mineral separates of clinopyroxenes and garnets from kimberlite pipes: P6 (clinopyroxenes), P7 (garnets), P1P2 (clinopyroxenes), P3P (garnet), P3 (clinopyroxene), P3D (garnets), P10 (garnet) and P1P2 (garnets).

Figure 3. Key major element distribution in mantle minerals. Large red symbols are results from this study, small red symbols are from previous studies for Dharwar craton (Ganguly and Bhattacharya, 1987 and Nehru and Reddy, 1989; and Shaikh et al., 2020) and small grey symbols are from previous studies for peridotite xenoliths from others cratons: Canada (Kopylova et al., 1999; MacKenzie and Canil, 1999; Menzies et al., 2004); Kaapvaal (Grégoire et al., 2005; Gibson et al., 2008; Lazarov et al., 2009; Konzett et al., 2013; Hanger et al., 2015; Bell et al., 2005); Siberia (Ionov et al., 2010; Doucet et al., 2012; 2014). (a) Mg# as a function of NiO contents (wt.%) in olivine; b) CaO content (wt.%) as a function of Al_2O_3 content (wt.%) in clinopyroxenes. (b) Mg# as a function of TiO_2 content (wt.%) in clinopyroxenes; and (d) Al_2O_3 contents (wt.%) as a function of Cr_2O_3 contents (wt.%) in garnet. Red squares are for eclogitic garnets from Eastern Dharwar craton (Dongre et al., 2015) and grey squares are for garnets from other eclogites transported by kimberlites from Koidu (Hills and Haggerty, 1989), Roberts Victor (MacGregor and Manton, 1986), Yakutia (Snyder et. al, 1997; Jerde et al., 1993; Sobolev et al., 1994).

1077

1078 **Figure 4**. Representative unpolarized infrared spectra for anhydrous nominally minerals from
1079 Wajrakarur; (a) olivine, (b) diopside, (c) orthopyroxenes, and (d) garnet. The integrated
1080 absorbance is reported for each spectrum of olivine, opx and cpx. The dotted lines represent the
1081 range of integration and the star symbol represents the contamination by hydrous minerals (see
1082 main text for details). All spectra have been normalized to 1 cm of thickness. Spectra from
1083 previous studies are shown for comparison.

1084

1085 **Figure 5.** Representative unpolarized infrared spectra for anhydrous nominally minerals from
1086 Wajrakarur contaminated by hydrous mineral lamellae. All spectra have been normalized to
1087 1 cm of thickness.

1088

1089 **Figure 6.** Hydrogen concentrations (express in ppm by weight of water) of olivine from
1090 Wajrakarur peridotites as a function of magnesium number [Mg# = 100 × Mg/(Mg+Fe)]. Full
1091 red symbol is for sample P3/6/3 olivine, while open symbols are the H concentration is the
1092 result of calculation using partitioning coefficient for samples P3/5/1 and P3/6/1 (see main text
1093 for values used in this study). For comparison data for other olivines are shown here: olivine
1094 megacrysts from Kaapvaal (Bell et al., 2004); peridotitic olivines from Kaapvaal (Peslier et al.,
1095 2010; Baptiste et al., 2012); olivine phenocrysts from Udachnaya (Kamenetsky et al., 2008);
1096 peridotitic olivines from Udachnaya (Doucet et al., 2014); off-craton spinel-bearing peridotites
1097 (Demouchy et al., 2015, Demouchy and Bolfan-Casanova, 2016, Denis et al., 2013, 2018; Li et
1098 al., 2008, NB: the spinel-lherzolites only).

1099

1100 **Figure 7.** (a) Ti concentrations in ppm determined by LA-ICP-MS as a function of the sum of
1101 the normalized integrated absorbance from the IR bands 3575 and 3525 cm^{-1}, which are

attributed to titanium clinohumite-like point defects (see main text for details). For comparison, results from experimental studies and data from natural mantle samples are also reported (S2013: Schmädicke et al., 2013; Dm2015: Demouchy et al., 2015; PN&H2017: Padrón-Navarta and Hermann, 2017; Dn2015: Denis et al., 2015; T2018: Tollan et al., 2018). (b) Compilation of Ti concentrations observed in peridotites together with data from O'Reilly et al. (1997); De Hoog et al. (2014); Peslier (2010); Peslier et al. (2012); Satsukawa et al. (2017) for comparison.

Figure 8. Hydrogen concentrations (express in ppm of water by weight) in clinopyroxenes from Wajrakarur peridotites as a function of Al_2O_3 contents (wt.%) in clinopyroxenes. For comparison, data for clinopyroxenes from a variety of tectonic settings are also shown. Clinopyroxenes in kimberlites from Premier Mine and Lesotho (Peslier et al., 2010); eclogites from the Alps and from Khazakstan (Katayama et al., 2006; Peslier, 2010), basalts from Nushan and Hannuoba (Yang et al., 2008); Massif central (Denis et al., 2015); Mexico (Peslier et al., 2002); Ichinomegata and Okidogo in Japan (Satsukawa et al., 2017).

Figure 9. Hydrogen concentrations (express in ppm of water by weight) in olivine from Wajrakarur peridotites as a function of depth (using two different geobarometers, BK: Brey and Kohler (1990) or NG: Nickel and Green (1985), see main text for details). Open symbols are values derived from partitioning coefficients. For comparison, data for olivines from two well-studied cratons are also shown: Kaapvaal (Peslier et al., 2010; Baptiste et al., 2012); and Udachnaya (Doucet et al., 2014). Hydrogen concentrations in olivine inclusion within diamonds are also shown for comparison (Novella et al., 2015 by FTIR and Jean et al., 2016 by secondary ion mass spectrometry). Matsyuk and Langer (2004) reported two dry olivines within diamond, but without pressure of equilibrium, which prevents us to implement these data in the

figure. We encountered the same problem for olivine inclusion in diamonds from Taylor et al. (2016).

Pattnaik et al., Fig. 1

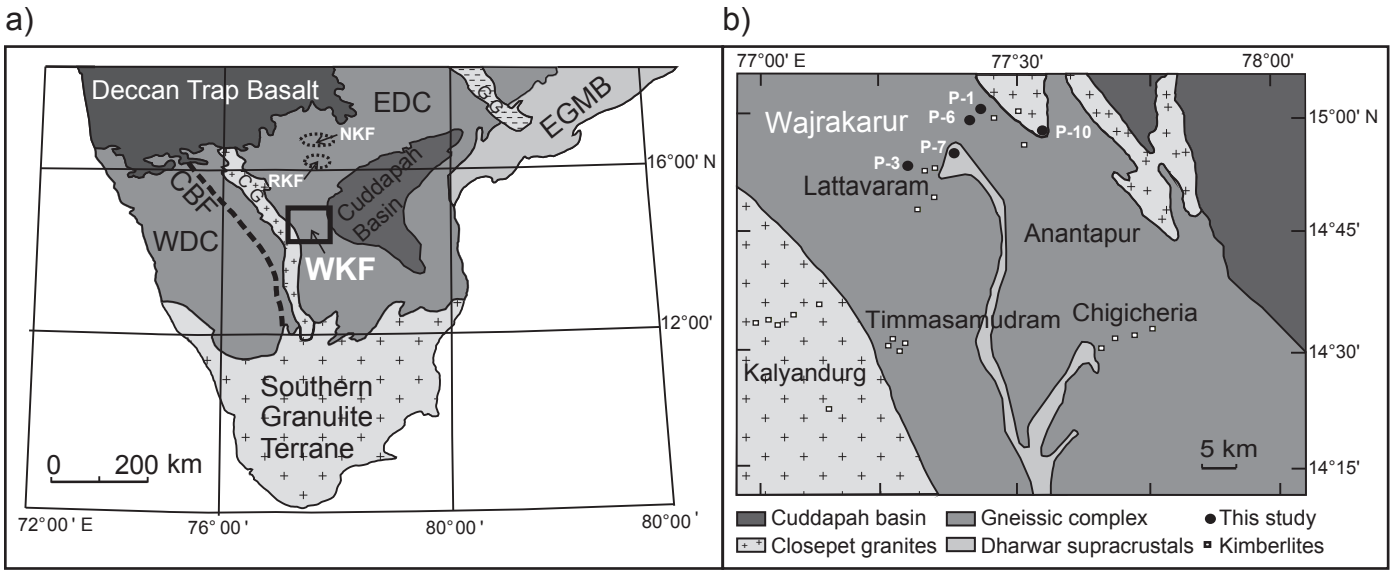

Fig. 2. Pattnaik et al.

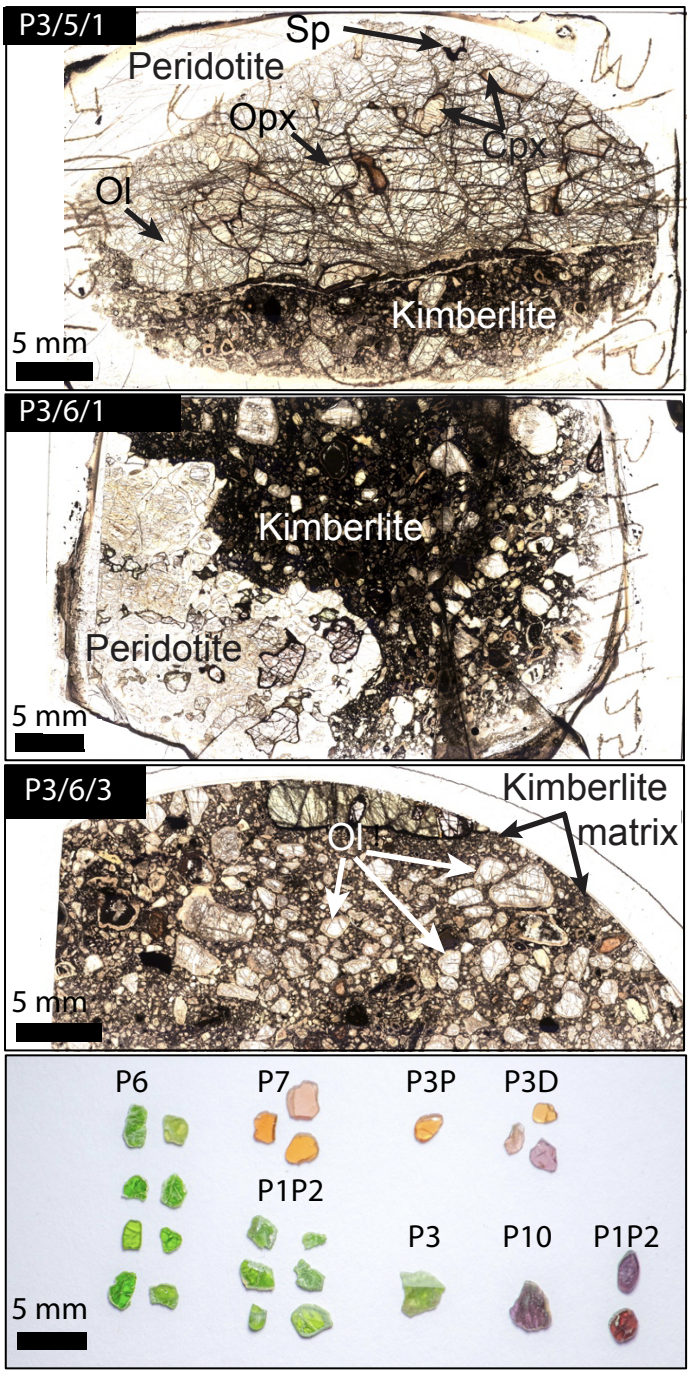

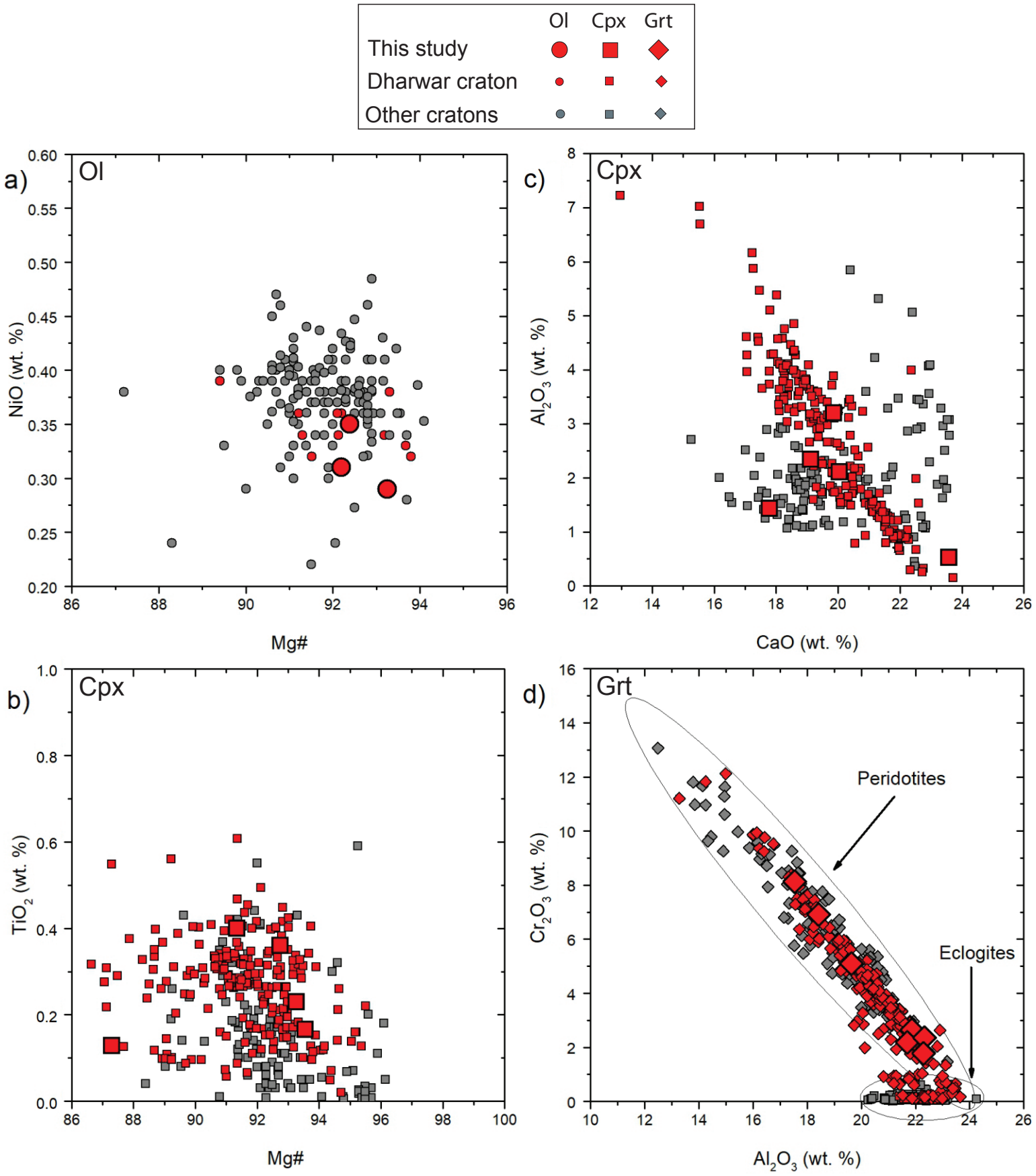
Ol
Cpx
Grt
This study
Dharwar craton
Other cratons
a)
Ol
NiO (wt. %)
Mg#
c)
Cpx
Al2O3 (wt. %)
CaO (wt. %)
b)
Cpx
TiO2 (wt. %)
Mg#
d)
Grt
Cr2O3 (wt. %)
Al2O3 (wt. %)
Peridotites
Eclogites

Fig. 4
Pattnaik et al.,

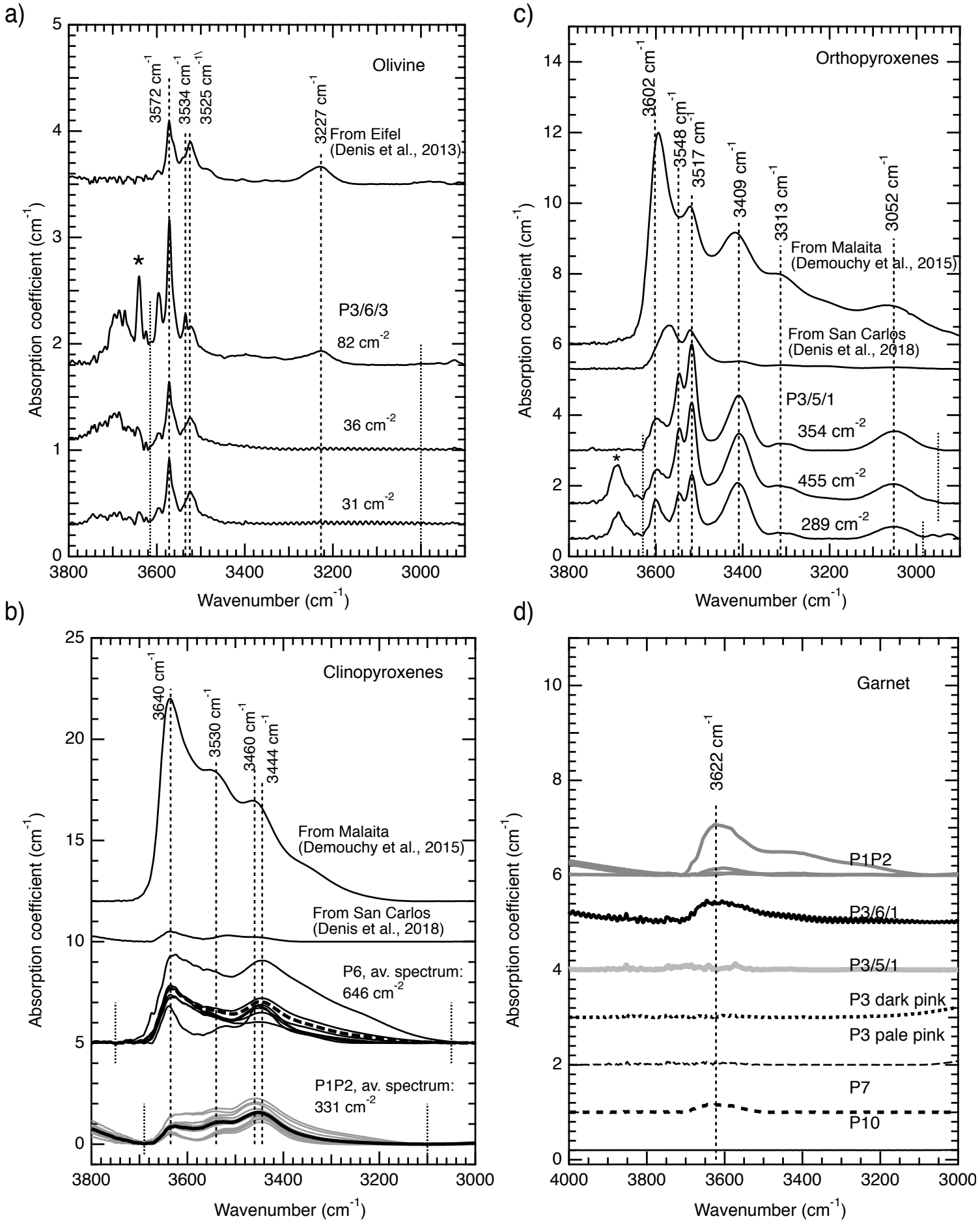

Fig. 5
Pattnaik et al.,

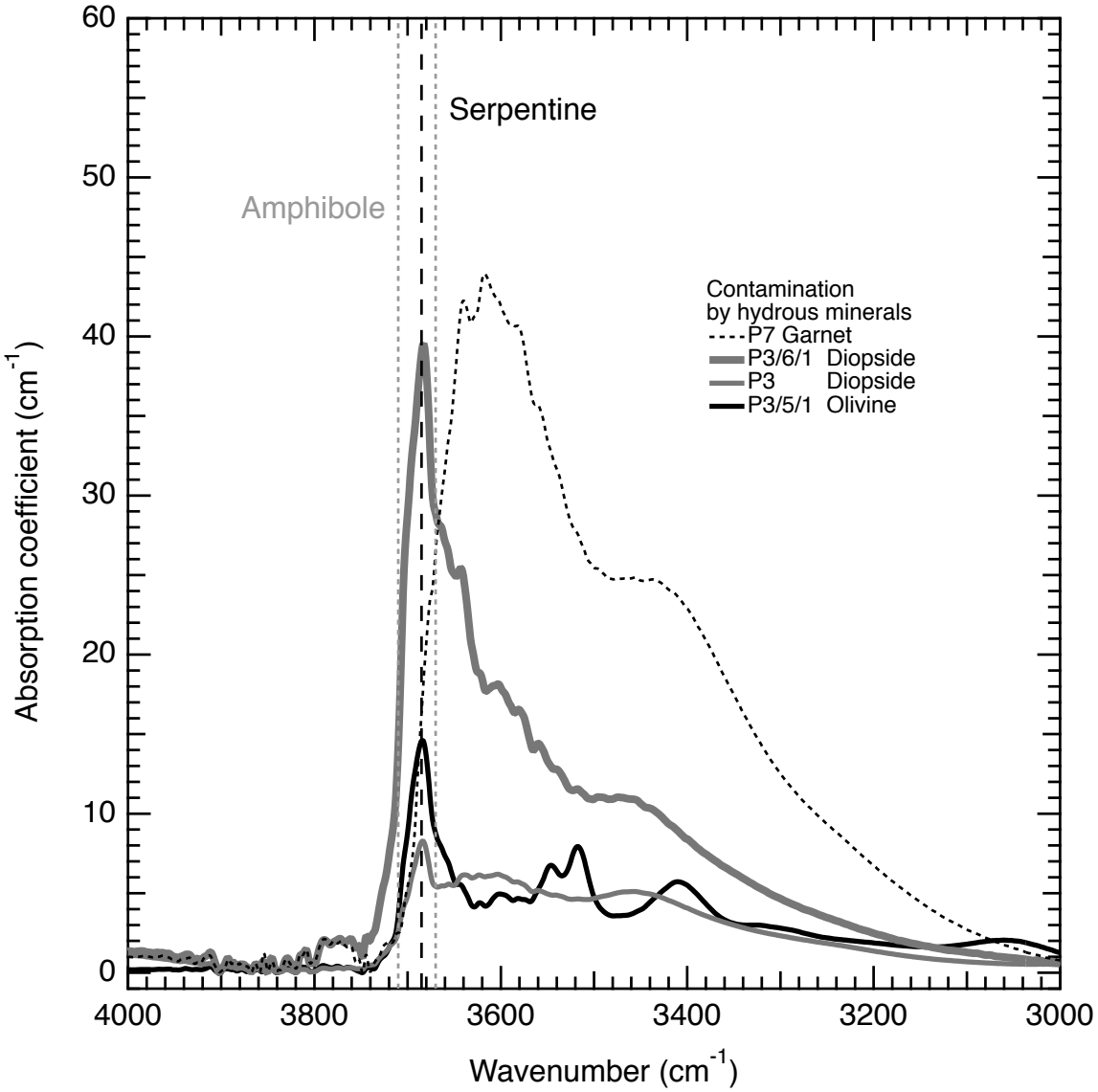

Fig. 6 revised
Pattnaik et al.,

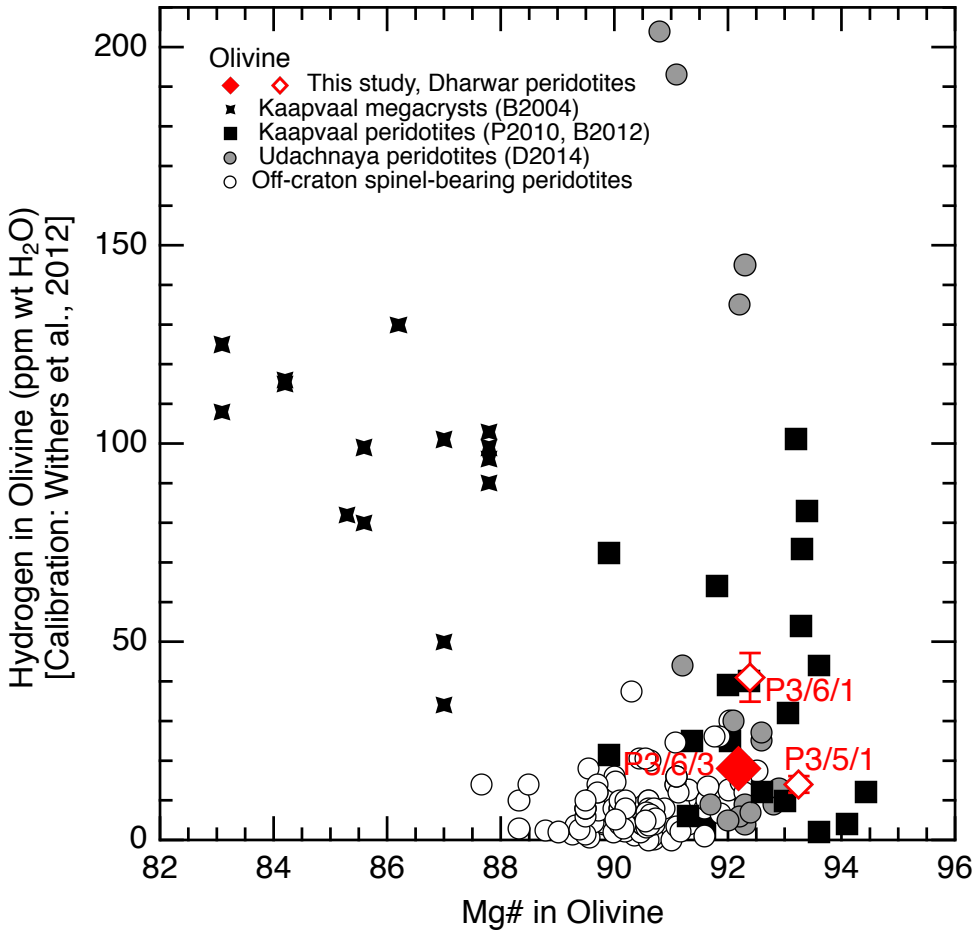

Figure 7, Pattnaik et al.

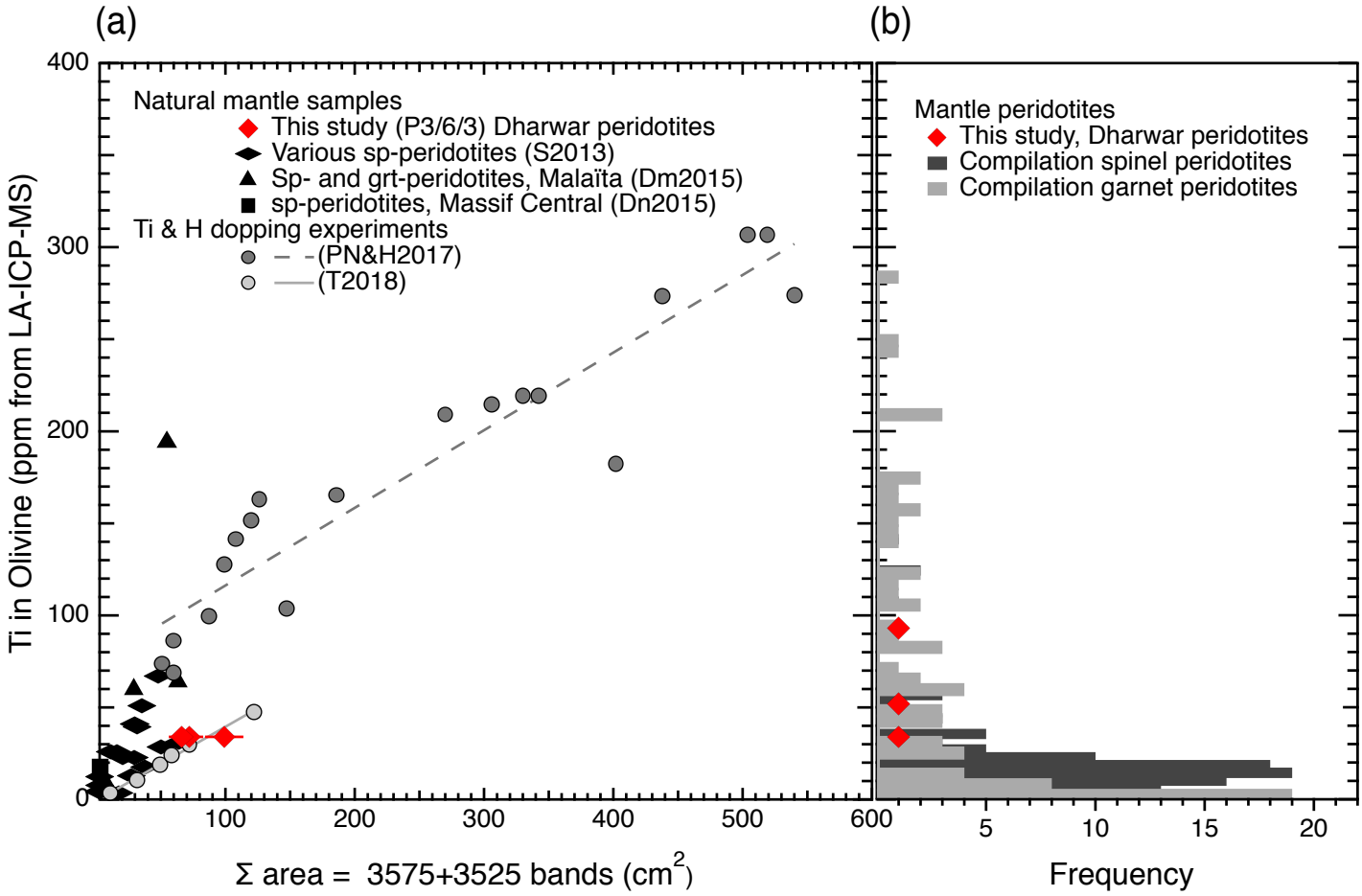

Fig. 8
Pattnaik et al.

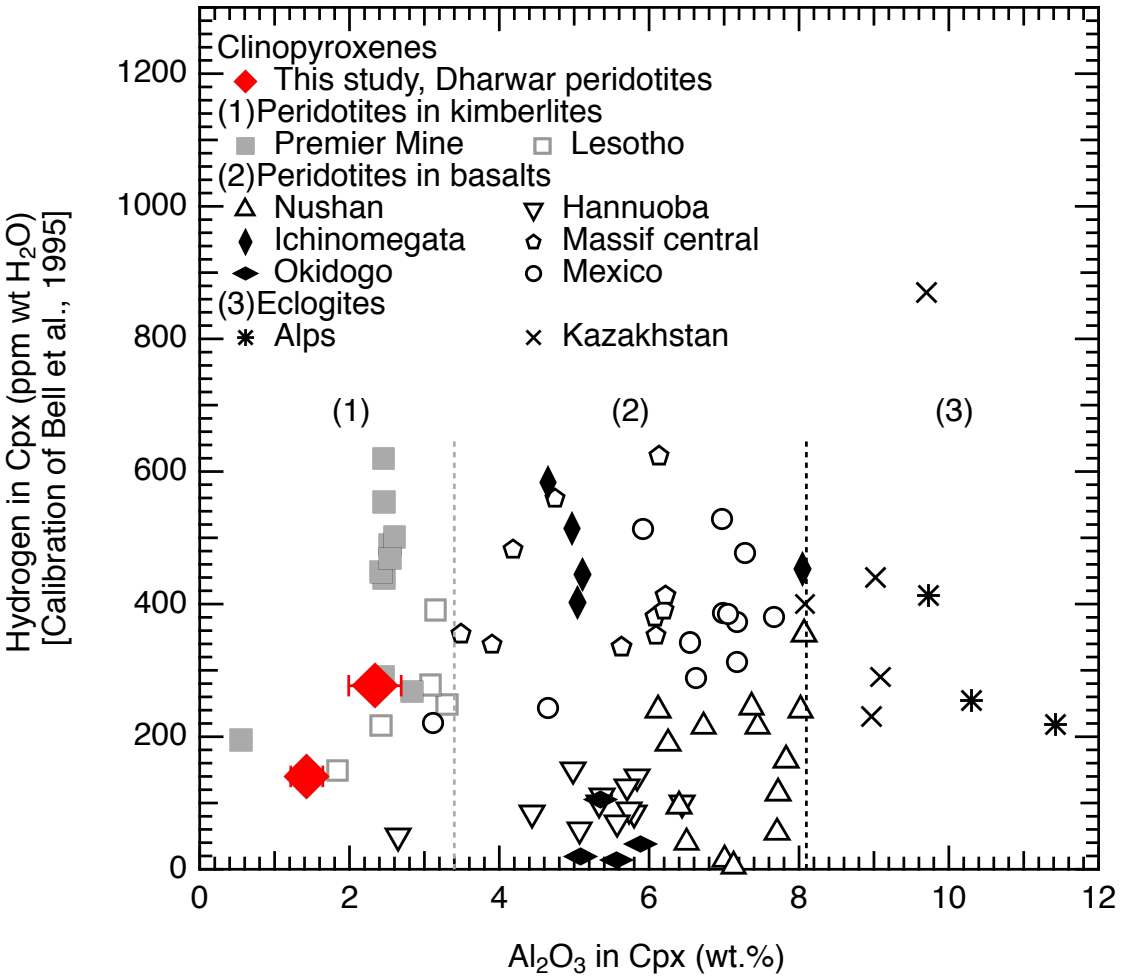

Fig. 9, Pattnaik et al.

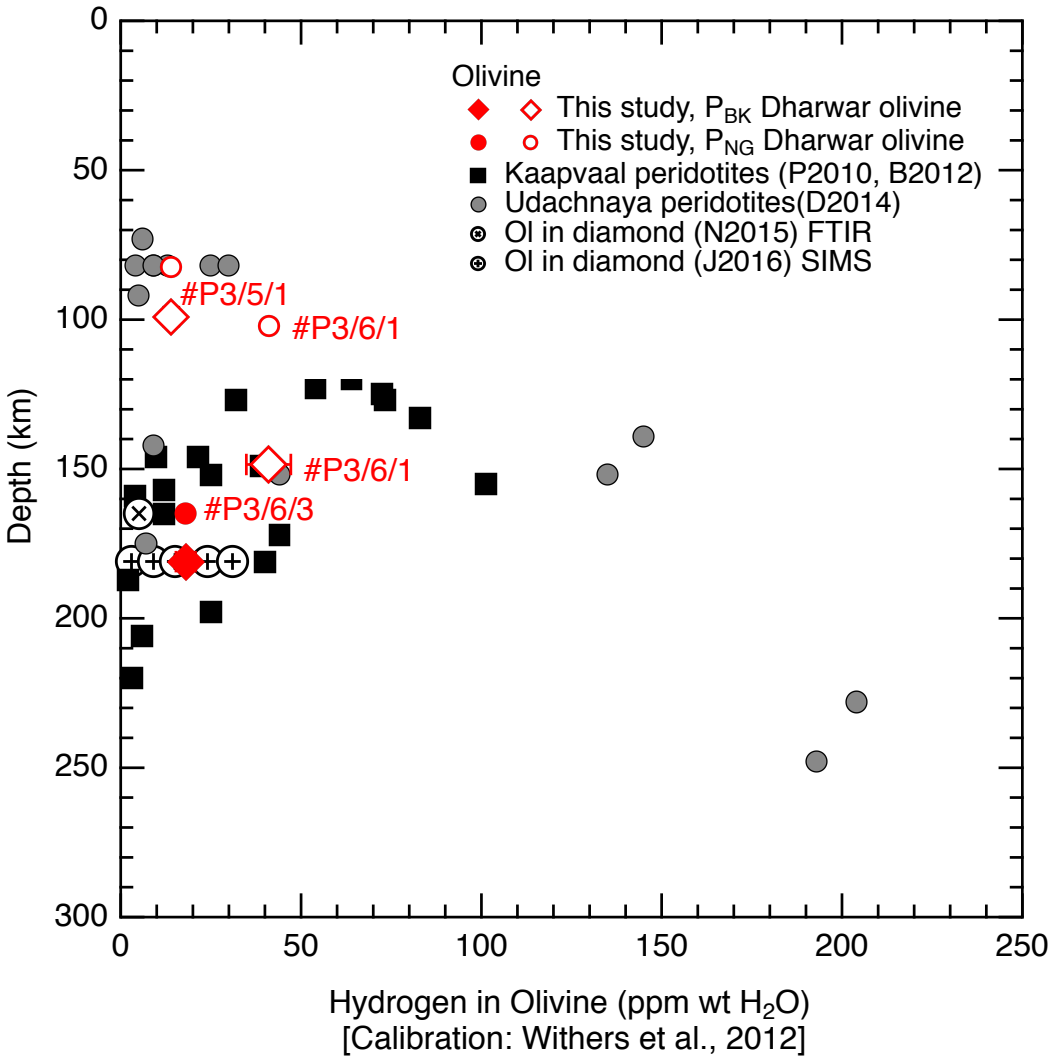

Table 1. Sample types, mineral modes and estimated equlibrium temperatures and pressures for peridotites and mantle minerals from Dharwar craton.

Sample no.	Location	Sample Type	Rock type/Mineral	Mineral modes (vol.%)	T_{BK90} (°C)	P_{NG} (GPa)	T_{TA} (°C)	P_{NG} (GPa)
P3/5/1	Pipe 3	Mantle xenolith	Spinel ±Garnet Lherzolite	$Ol_{77}Opx_{15}Cpx_{7}Sp_{1}$	940	3.0	710	2.5
P3/6/1	Pipe 3	Mantle xenolith	Garnet Lherzolite	$Ol_{74}Opx_{13}Cpx_{9}Grt_{4}$	1050	4.5	831	3.1
P3/6/3*	Pipe 3	Mantle mineral	Olivine grains in matrix	3 grains	1270	5.5	1179	5
P1P2	Pipe 1	Mineral separated from mantle xenolith	Diopside	6 grains	n.d.	n.d.	n.d.	n.d.
P1P2	Pipe 1	Mineral separated from mantle xenolith	Garnet	2 grains	n.d.	n.d.	n.d.	n.d.
P3D	Pipe 3	Mineral separated from mantle xenolith	Garnet	3 grains	n.d.	n.d.	n.d.	n.d.
P3P	Pipe 3	Mineral separated from mantle xenolith	Garnet	1 grains	n.d.	n.d.	n.d.	n.d.
P3	Pipe 3	Mineral separated from mantle xenolith	Diopside	1 grain	n.d.	n.d.	n.d.	n.d.
P6	Pipe 6	Mineral separated from mantle xenolith	Diopside	8 grains	n.d.	n.d.	n.d.	n.d.
P7	Pipe 7	Mineral separated from mantle xenolith	Garnet	3 grains	n.d.	n.d.	n.d.	n.d.
P10	Pipe 10	Mineral separated from mantle xenolith	Garnet	1 grain	n.d.	n.d.	n.d.	n.d.

Ol - olivine; Cpx - clinopyroxene; Opx - orthopyroxene; Sp - spinel; Grt - Garnet

T_{BK90} - Brey and Kohler (1990); T_{TA} - Taylor (1998); P_{NG} - Nickel and Green (1985)

Temperatures (T_{TA}) and Pressures (P_{NG}) were calculated assumimg an initial pressure of 3 GPa for spinel peridotite and 5 GPa for garnet peridotites.

* Garnet was not present in this section, we assumed 5 vol. % of garnet as observed in samples from the same pit (Ganguly and Bhattacharya, 1987).

Table 2. Typical average major, minor and trace element compositions of mantle minerals from Dharwar craton ; n gives the number of analysed EPMA points to obtain the reported average values. Between 2 and 9 points were analyzed by LA-ICP-MS. Mg#=100×Mg/(Mg+Fe) in atomic ratio and Cr#= 100×Cr/(Cr+Al). NB: EPMA analyses were performed on thin section while FTIR were performed on thick hand polished grains and sections.

Sample no.	P3/5/1								P3/6/1								P3/6/3	
Minerals	Ol		Opx		Cpx		Spl		Ol		Opx		Cpx		Grt		Ol	
wt.%	n=8	σ	n=25	σ	n=4	σ	n=6	σ	n=5	σ	n=2	σ	n=8	σ	n=9	σ	n=12	σ
SiO_2	41.3	(0.3)	57.6	(0.4)	53.0	(0.3)	0.03	(0.03)	40.8	(0.5)	57.4	(0.1)	53.3	(0.8)	41.8	(0.4)	41.0	(0.7)
TiO_2	0.00	(0.00)	0.00	(0.01)	0.17	(0.01)	0.00	(0.01)	0.02	(0.03)	0.13	(0.03)	0.36	(0.07)	0.22	(0.03)	0.01	(0.02)
Al_2O_3	0.01	(0.00)	0.96	(0.04)	0.50	(0.3)	17.3	(0.3)	0.03	(0.02)	0.96	(0.01)	3.20	(0.3)	21.90	(0.3)	0.01	(0.01)
Cr_2O_3	0.03	(0.02)	0.31	(0.05)	0.30	(0.1)	53.8	(0.5)	0.01	(0.01)	0.33	(0.00)	1.80	(0.1)	2.70	(0.2)	0.02	(0.03)
FeO	6.80	(0.2)	4.30	(0.2)	2.30	(0.4)	15	(0.3)	7.60	(0.30)	4.60	(0.10)	2.30	(0.2)	7.10	(0.1)	7.60	(3.7)
MnO	0.08	(0.25)	0.10	(0.2)	0.02	(0.03)	0.3	(0.1)	0.09	(0.06)	0.08	(0.08)	0.07	(0.07)	0.33	(0.06)	0.13	(0.08)
MgO	52.61	(0.01)	37.00	(0.02)	18.50	(0.9)	13.9	(0.2)	51.8	(0.67)	36.00	(0.10)	16.30	(0.5)	21.90	(0.2)	50.00	(3)
CaO	0.04	(0.02)	0.19	(0.05)	23.00	(1)	0.01	(0.01)	0.02	(0.02)	0.44	(0.06)	19.90	(1)	4.60	(0.08)	0.04	(0.02)
Na_2O	0.01	(0.01)	0.02	(0.01)	0.5	(0.1)	0.01	(0.01)	0.01	(0.01)	0.14	(0.01)	2.40	(0.8)	0.07	(0.02)	0.02	(0.02)
K_2O	0.00	(0.00)	0.01	(0.00)	0.7	(0.5)	0.01	(0.01)	0.01	(0.01)	0.00	(0.00)	0.02	(0.03)	0.00	(0.01)	0.01	(0.01)
NiO	0.29	(0.01)	0.10	(0.01)	0.04	(0.01)	0.06	(0.01)	0.35	(0.01)	0.04	(0.01)	0.03	(0.01)	0.00	(0.01)	0.31	(0.01)
Total	101.18		100.58		99.04		100.42		100.78		100.13		99.66		100.60		99.10	
Mg#	93.3		93.9		93.6				92.4		93.3		92.7				92.2	
Cr#	-		17.7		24.4				-		18.7		27.5				-	
ppm	n=2		n=1		n=1		n=1		n=2		n=2		n=3		n=2		n=2	
Ni	2932	(277)	864		344.00		532		2932	(39)	864	(62)	270	(7)	31	(2.8)	2492	(356)
Mn	716	(44)	432		762.00		1301		716	(3)	431	(21)	499	(26)	2629	(125)	676	(9)
Na	18	(3)	23		1142.82		b.d.l		63	(18)	286	(24)	17547	(39)	371	(77)	56	(75)
Ti	52	(4)	4		1319.00		62		93	(3)	11	(5)	1678	(20)	1583	(421)	34	(64)
La	b.d.l		b.d.l		2.04		0.02		b.d.l		b.d.l	b.d.l	26.00	(2)	0.06	(0.03)	b.d.l	
Ce	b.d.l		0.02		41.23		0.52		b.d.l		b.d.l	b.d.l	78.00	(5)	0.76	(0.16)	b.d.l	
Li	n.d.		n.d.		n.d.		n.d.		n.d.		n.d.		n.d.		n.d.		n.d.	
V	2.45	(0.06)	33		501		2045		5.60	(0.2)	15	(2.83)	560	(8.85)	242	(70)	b.d.l	b.d.l

Sample no.	P1P2		P1P2		P3D		P3P		P3		P6		P7-1		P7-2		P10	
Minerals	Di		Grt		Grt		Grt		Di		Di		Grt		Grt		Grt	
wt.%	n=22	σ	n=4	σ	n=6	σ	n=4	σ	n=2	σ	n=4	σ	n=3	σ	n=3	σ	n=4	σ
SiO_2	54.9	(0.2)	42.8	(0.3)	42.3	(0.3)	43.2	(0.2)	55.7	(0.1)	55.5	(0.3)	41.6	(0.7)	41.1	(0.3)	42.3	(0.3)
TiO_2	0.13	(0.03)	0.16	(0.03)	0.29	(0.04)	0.25	(0.02)	0.40	(0.01)	0.23	(0.06)	0.07	(0.02)	0.02	(0.00)	0.21	(0.01)
Al_2O_3	1.43	(0.06)	21.71	(0.03)	22.30	(0.5)	22.30	(0.4)	2.10	(0.02)	2.30	(0.2)	19.70	(0.3)	17.50	(0.1)	18.40	(069)
Cr_2O_3	1.00	(0.1)	2.20	(0.1)	2.35	(0.66)	1.80	(0.7)	0.60	(0.20)	2.55	(0.55)	5.10	(0.26)	8.12	(0.02)	6.90	(0.8)
FeO	3.00	(0.2)	6.50	(0.1)	7.00	(0.9)	6.96	(0.05)	2.98	(0.2)	2.15	(0.02)	5.40	(0.1)	5.56	(0.51)	6.50	(0.3)
MnO	0.10	(0.07)	0.25	(0.13)	0.30	(0.07)	0.32	(0.06)	0.06	(0.08)	0.07	(0.04)	0.26	(0.13)	0.32	(0.04)	0.40	(0.1)
MgO	20.50	(0.3)	22.00	(0.10)	22.20	(0.7)	21.90	(0.2)	17.60	(0.1)	16.80	(0.2)	22.90	(0.4)	22.01	(0.01)	19.80	(0.6)
CaO	17.80	(0.5)	4.59	(0.04)	4.20	(0.3)	4.35	(0.10)	20.00	(0.20)	19.10	(0.3)	4.26	(0.06)	5.07	(0.01)	6.50	(0.5)
Na_2O	0.88	(0.04)	0.05	(0.02)	0.07	(0.10)	0.05	(0.01)	1.43	(0.02)	2.10	(0.2)	0.03	(0.03)	0.01	(0.00)	0.03	(0.01)
K_2O	0.04	(0.01)	0.04	(0.01)	0.01	(0.01)	0.01	(0.01)	0.03	(0.01)	0.03	(0.01)	0.00	(0.00)	0.00	(0.00)	0.00	(0.00)
NiO	0.05	(0.01)	0.01	(0.01)	0.00	(0.01)	0.01	(0.01)	0.12	(0.01)	0.05	(0.01)	0.01	(0.01)	0.01	(0.01)	n.d	n.d
Total	99.84		100.28		101.00		101.17		101.06		100.94		99.34		99.74		101.02	
Mg#	92.4		85.8		84.9		84.9		91.4		93.3		88.3		87.6		84.5	
Cr#	32.3		6.3		6.6		5.1		16.7		42.2		14.8		23.7		20.1	
ppm	n=6		n=3		n=2		n=1		n=1		n=2		n=2		n=2			
Ni	396	60	111	(9)	48	(21)	51		924		381	(69)	89	(7)	65	(23)	n.d.	
Mn	753	(129)	2267	(123)	2763	(451)	2496		940		742	(57)	2071	(73)	3092	(71)	n.d.	
Na	3770	(90)	255	(23)	428	(158)	511		17782		15253	(1306)	60	(3)	514	(154)	n.d.	
Ti	875	(53)	1280	(305)	2544	(317)	1976		1066		758	(63)	294	(19)	274	(53)	n.d.	
La	1.2	(0.9)	b.d.l	b.d.l	b.d.l	b.d.l	0.0		10.9		11.5	(4)	0.1	(0.06)	b.d.l	b.d.l	n.d.	
Ce	6.0	(3)	0.4	(0.05)	0.3	(0.2)	0.3		35.2		35.0	(19)	0.8	(0.4)	0.2	(0.07)	n.d.	
Li	2.7	(0.4)	0.0	(0.00)	0.1	(0.10)	0.3		3.4		1.0	(0.4)	n.d.		n.d.		n.d.	
V	154	(80)	15	(6)	236	(42)	134		325		464	(71)	333	(42)	100.0	(30)	n.d.	

Table 3: Integrated normalized absorbance and hydrogen concentrations for the-mineral grains from this study

Sample	Thickness (mm ± 0.001)	Mineral phase	Int. Abs. Coeff. (cm^{-2})	Paterson (1982) (ppm wt H_2O) 2σ=30%	Garnet or Pyroxenes Bell et al. (1995) (ppm wt H_2O) 2σ=20-30%	Olivine - Withers et al. (2012) (ppm wt H_2O) 2σ=10%
			Thin sections			
P3/5/1	0.211	Orthopyroxene	455	77	88	-
P3/5/1	0.211	Orthopyroxene1	354	64	68	-
P3/5/1	0.211	Orthopyroxene2	289	53	56	-
P3/5/1	0.211	**Orthopyroxene (average)**	**366**	**65**	**70**	
P3/5/1	0.211	Garnet	Dry	Dry	-	-
P3/6/1	0.216	Diopside	contaminated	-	-	-
P3/6/1	0.216	Garnet	88	75	63	-
P3/6/3	0.211	Olivine1	82	18	-	29
P3/6/3	0.211	Olivine2	36	8	-	13
P3/6/3	0.211	Olivine3	31	7	-	11
P3/6/3	0.211	**Olivine (average)**	**50**	**11**	**-**	**18**
			Mineral separated from mantle xenolith			
P1P2	0.390	Diopside1 position1	318	69	135	-
P1P2	0.390	Diopside1 position2	355	73	150	-
P1P2	0.390	Diopside1 position3	320	69	135	-
P1P2	0.390	Diopside2 position1	282	61	119	-
P1P2	0.390	Diopside2 position2	355	77	150	-
P1P2	0.390	Diopside2 position3	325	66	138	-
P1P2	0.390	Diopside3 position1	192	40	81	-
P1P2	0.390	Diopside3 position3	162	34	69	-
P1P2	0.390	Diopside3 position4	193	39	82	-
P1P2	0.390	Diopside4 position1	209	41	88	-
P1P2	0.390	Diopside5 position1	449	91	190	-
P1P2	0.390	Diopside6 position1	602	122	255	-
P1P2	0.390	Diopside6 position2	603	122	255	-
P1P2	0.390	**Diopside (average)**	**335**	**69**	**142**	-
P1P2	0.590	Garnet1	359	54	258	-
P1P2	0.590	Garnet1	21	5	15	-
P1P2	0.590	Garnet2	Dry	Dry	-	-
P3	0.241	Diopside	contaminated	-	-	-
P3	0.458	Garnet	Dry	Dry	-	-
P3D	0.351	Garnet	Dry	Dry	-	-
P3D	0.351	Garnet	Dry	Dry	-	-
P3D	0.351	Garnet	Dry	Dry	-	-
P6	0.336	Diopside1	*528*	124	223	-
P6	0.336	Diopside2	481	118	204	-
P6	0.336	Diopside3	1518	309	642	-
P6	0.336	Diopside4	308	71	130	-
P6	0.336	Diopside5	497	107	210	-
P6	0.336	Diopside6	726	162	307	-
P6	0.336	Diopside7	463	122	196	-
P6	0.336	**Diopside (average)**	**646**	**145**	**273**	-
P7	0.372	Garnet1	Dry	Dry	-	-
P7	0.372	Garnet2	Dry	Dry	-	-
P7	0.372	Garnet3	19	6	14	-
P10	0.492	Garnet	Dry	Dry	-	-